ijrr

Five-degree-of-freedom manipulation of an untethered magnetic device in fluid using a single permanent magnet with application in stomach capsule endoscopy

Arthur W. Mahoney[1] and Jake J. Abbott[2]

Abstract

This paper demonstrates magnetic three-degree-of-freedom (3-DOF) closed-loop position and 2-DOF open-loop orientation control of a mockup magnetic capsule endoscope in fluid with a single permanent magnet positioned by a commercial 6-DOF robotic manipulator, using feedback of only the 3-DOF capsule position measured by a localization system, with application in capsule endoscopy of a fluid-distended stomach. We analyze the kinematics of magnetic manipulation using a single permanent magnet as the end-effector of a serial-link robot manipulator, and we formulate a control method that enables the capsule's position and direction to be controlled when the robot manipulator is not in a kinematic singularity, and that sacrifices control over the capsule's direction to maintain control over the capsule's position when the manipulator enters a singularity. We demonstrate the method's robustness to a reduced control rate of 25 Hz, reduced localization rates down to 30 Hz, deviation in the applied magnetic field from that expected, and the presence of manipulator singularities. Five-DOF manipulation of an untethered magnetic device has been previously demonstrated by electromagnetic systems only.

Keywords

Magnetic manipulation, capsule endoscopy, medical robotics

1. Introduction

Untethered devices that derive their power from externally applied magnetic fields have been an active area of research due to their potential for accessing hard-to-reach areas of the human body (Gillies et al., 1994; Nelson et al., 2010). These devices, which consist of a magnetic body rigidly attached to a functional structure, are particularly promising for use in the gastrointestinal (GI) system, where an untethered magnetic capsule endoscope could be used to actively image the GI system, making current GI screening procedures faster, safer, and less invasive (Valdastri et al., 2012b). Untethered magnetic devices range in size from the microscale to the mesoscale and are being applied to surgical tasks in the eye (Kummer et al., 2010), in vasculature (Martel et al., 2007), and other hard-to-reach areas of the human body (Ishiyama et al., 2003; Mahoney et al., 2012). Irrespective of application, untethered magnetic devices are often viewed as end-effectors to a larger robotic system that could consist of an arrangement of stationary electromagnets, or in the case of this paper, a single permanent magnet positioned in space with a robot manipulator.

There exist a variety of methods for employing magnetic force and/or magnetic torque to control untethered magnetic devices. Some methods apply magnetic force for pulling (Gauthier and Piat, 2006; Ciuti et al., 2010b; Keller et al., 2010; Swain et al., 2010; Lien et al., 2012; Tognarelli et al., 2012; Valdastri et al., 2012a; Arezzo et al., 2013). Others employ magnetic torque to generate rotation that is converted into propulsion by rolling (Hou et al., 2010; Jiang et al., 2010; Mahoney and Abbott, 2011; Yim and Sitti, 2012) or through a chiral structure (Ishiyama et al., 2003; Zhang et al., 2009; Fountain et al., 2010; Mahoney et al., 2011; Kim et al., 2012). Magnetic force and torque can also be applied simultaneously toward direct propulsion (Mahoney and Abbott, 2014b).

[1]School of Computing, University of Utah, USA
[2]Department of Mechanical Engineering, University of Utah, USA

Corresponding author:
Arthur W. Mahoney, School of Computing, University of Utah, Salt Lake City, UT, 84112 USA.
Email: art.mahoney@utah.edu

Irrespective of the form of propulsion, an untethered device containing a single permanent magnet can be controlled with at most five degrees of freedom (DOFs), without additional externally applied nonmagnetic forces. To date, three electromagnetic systems have been developed with the ability to perform 5-DOF magnetic manipulation: the OctoMag (Kummer et al., 2010) and Magnetecs (Nguyen et al., 2010) systems consist of eight ferromagnetic-core electromagnets arranged around a hemisphere and sphere, respectively, directed inward toward the manipulation workspace, and a system developed jointly by Olympus and Siemens, consisting of 12 electromagnets through which a patient is positioned, for the control of a magnetic capsule endoscope in a water-filled stomach (Keller et al., 2012). The OctoMag system, and similar designs, have been used to control a millimeter-scale untethered device in the eye (Ullrich et al., 2013), nanostructures in fluid (Schuerle et al., 2013), and multiple, heterogeneous, millimeter-scale devices in an independent fashion (Diller et al., 2013). The Magnetecs system has been used to steer a magnetic cardiac catheter in in vivo porcine experiments (Gang et al., 2011). The Olympus–Siemens system has been used in in vivo porcine experiments and human clinical trials (Rey et al., 2010, 2012; Mewes et al., 2013). Six-DOF electromagnetic control of an untethered device containing two non-collocated permanent magnets has been demonstrated in Berkelman and Dzadovsky (2013). The work presented in this paper focuses on the control of devices that contain one permanent magnet.

Compared to electromagnetic actuation systems, permanent-magnet systems are desirable in that they generate magnetic fields that can apply clinically relevant forces and torques to a magnetic device, inexpensively and in a compact form-factor. Whereas electromagnetic systems can be designed to generate magnetic fields that are easy to control, permanent-magnet systems (particularly those that employ a single permanent magnet) have been hindered by the complex geometry of the dipole field that they produce. Actuation strategies that employ a single permanent magnet can be classified into two categories: those that use continuously rotating magnetic fields and those that do not.

Continuously rotating magnetic fields can be produced by continuously rotating a permanent magnet. Actuation methods that employ continuously rotating fields generally propel via rolling or helical propulsion using magnetic torque, which is continuously generated by the rotating magnetic field. In Hou et al. (2010) and Jiang et al. (2010), a microscale untethered magnetic device is made to roll on a surface using a rotating permanent magnet. In Yim and Sitti (2012), a rotating permanent magnet is used to roll a centimeter-scale soft-endoscope device in the interior of a stomach simulator. Other work has employed a rotating permanent magnet to drive a mockup capsule endoscope, functionalized with a helical thread, and a helical swimmer in a lumen (Fountain et al., 2010; Kim et al., 2012; Mahoney and Abbott, 2014b).

In the preceding examples, the magnetic force generated between the rotating magnetic device and the rotating permanent magnet tends to attract the device toward the rotating magnet. By rotating the actuator magnet in a specific, predefined manner, Mahoney and Abbott (2011) demonstrated that the magnetic force applied to a rolling device can be directed laterally in the direction of propulsion (perpendicular to the attractive direction). Fountain et al. employed a rotating permanent magnet to actuate millimeter-scale helical swimmers through a lumen and demonstrated that in specific configurations the applied magnetic force can be eliminated when rotating the permanent magnet actuator at the highest frequency that the swimmer can remained synchronized (Fountain et al., 2010). A generalized model that predicts both of the phenomena described above was developed in Mahoney et al. (2013).

Methods of actuation that do not employ continuously rotating fields utilize the applied magnetic force produced between the actuator magnet and the untethered device for propulsion via dragging and orient the untethered device using the applied magnetic torque. In Keller et al. (2010, 2011), Swain et al. (2010) and Lien et al. (2012), a permanent magnet is positioned by hand to drag a capsule endoscope in the human esophagus and stomach. In similar work to that presented herein, a permanent magnet is maneuvered by a robot manipulator for the control of an untethered capsule endoscope (Ciuti et al., 2010a,b; Valdastri et al., 2012a). A similar system is used in Tognarelli et al. (2012) to demonstrate pulling an untethered device through vasculature with the addition of a second robot manipulator used to obtain ultrasound position feedback. Whether the actuator magnet is positioned manually or using a robot manipulator, all prior work has achieved at most 4-DOF control over the untethered device (i.e. 2-DOF orientation control and 2-DOF position control), since the untethered device always must be in contact with a tissue surface.

In this paper, we present a demonstration of 2-DOF orientation and 3-DOF position control of a mockup magnetic capsule endoscope in fluid using a single permanent magnet maneuvered by a robotic manipulator (5-DOF magnetic manipulation has been previously demonstrated by electromagnetic systems only). The magnetic force controls the *total* force (the sum of forces due to gravity, buoyancy, and the magnetics) acting on the capsule and thus the capsule's position, while the applied magnetic torque controls the capsule's heading. The magnetic force and torque are controlled by adjusting the position and orientation of the actuator magnet using only knowledge of the 3-DOF capsule position, obtained with a localization system. The mockup capsule is actuated in fluid, which simulates the environment of a fluid-distended stomach (pre-procedure consumption of fluid, rather than air insufflation, has been used successfully in human trials to open gastric folds for visualization during magnetic capsule endoscopy; Rey et al., 2010, 2012). A preliminary form of this work appeared in Mahoney and Abbott (2013) and in a more

detailed form in Mahoney and Abbott (2014a). This paper includes additional analysis and a detailed description of a control strategy that incorporates the physical limitations of the robot manipulator used to maneuver the actuator magnet. We demonstrate the control method's robustness to reduced capsule localization rates (down to 30 Hz) and deviation of the applied magnetic field from that expected, while updating the actuator magnet's pose at 25 Hz. Although the work presented herein is targeted at magnetic capsule endoscopy in a fluid-filled stomach, the methods can be applied to magnetic manipulation in general.

2. Control with a single permanent magnet

We follow the convention where scalars are denoted by lower-case, standard font (e.g. c), vectors are denoted in lower-case, bold font (e.g. $\mathbf{x}$), and matrices are denoted by capital, standard font (e.g. M). Unit vectors are denoted with the 'hat' symbol (e.g. $\hat{\mathbf{x}}$), and time derivatives are denoted by the 'dot' symbol (e.g. $\dot{\mathbf{x}}$). Nondimensionalized variables are denoted by the 'tilde' symbol (e.g. $\tilde{c}$ for scalars, $\tilde{M}$ for matrices).

The capsule endoscope is assumed to contain a permanent magnet, positioned at the capsule's center of gravity, with its dipole moment (i.e. the vector from the south to north pole) denoted by $\mathbf{m_c} \in \mathbb{R}^3$ in units A·m², which is assumed to be parallel to the capsule's principle axis. The actuator magnet's dipole moment is denoted by $\mathbf{m_a} \in \mathbb{R}^3$ and is positioned by a robotic manipulator with at least five DOFs; rotation of the actuator magnet about $\mathbf{m_a}$ is of no value, due to the axial symmetry of the dipole field. The positions of the actuator and capsule-endoscope magnet centers are denoted by $\mathbf{p_a} \in \mathbb{R}^3$ and $\mathbf{p_c} \in \mathbb{R}^3$, respectively, in units m.

We assume that the magnetic field $\mathbf{h}(\mathbf{p}, \hat{\mathbf{m}}_\mathbf{a}) \in \mathbb{R}^3$ generated by the actuator magnet can be modeled by the point-dipole model, which is given by

$$\mathbf{h}(\mathbf{p}, \hat{\mathbf{m}}_\mathbf{a}) = \frac{\|\mathbf{m_a}\|}{4\pi\|\mathbf{p}\|^3} D(\hat{\mathbf{p}})\hat{\mathbf{m}}_\mathbf{a} \qquad (1)$$

where $\mathbf{p} = \mathbf{p_c} - \mathbf{p_a}$ is the vector from the center of the actuator magnet to the center of the capsule's magnet (i.e. the relative position), $D(\hat{\mathbf{p}}) = 3\hat{\mathbf{p}}\hat{\mathbf{p}}^\mathrm{T} - I$, and $I \in \mathbb{R}^{3 \times 3}$ is the identity matrix. Since the magnitudes of $\mathbf{m_a}$ and $\mathbf{m_c}$ are constant (they are the dipole moments of *permanent* magnets), we express all functions of $\mathbf{m_a}$ and $\mathbf{m_c}$ as functions of $\hat{\mathbf{m}}_\mathbf{a}$ and $\hat{\mathbf{m}}_\mathbf{c}$ to explicitly indicate that their magnitudes do not vary. The field lines generated by the point-dipole model are shown in Figure 1(a). Equation (1) exactly predicts the field produced by a spherical magnet and is an approximation for every other geometry that becomes more accurate with increasing distance (Furlani, 2001). The geometry of a nonspherical magnet can be adjusted to make equation (1) a more accurate approximation in the near field (Petruska and Abbott, 2013). In this section, we assume that the dipole field accurately models the field of the actuator magnet.

The robot manipulator's n revolute and prismatic joint velocities $\dot{\mathbf{q}} \in \mathbb{R}^n$, in units of rad/s and m/s, respectively, are mapped to the actuator magnet's spatial $\dot{\mathbf{p}}_\mathbf{a}$ and angular $\boldsymbol{\omega}_\mathbf{a}$ velocities by the robot manipulator Jacobian matrix $J_\mathcal{R}(\mathbf{q}) \in \mathbb{R}^{6 \times n}$:

$$\begin{bmatrix} \dot{\mathbf{p}}_\mathbf{a} \\ \boldsymbol{\omega}_\mathbf{a} \end{bmatrix} = J_\mathcal{R}(\mathbf{q})\dot{\mathbf{q}} \qquad (2)$$

The point-dipole field (1) is radially symmetric about the actuator dipole moment and any component of $\boldsymbol{\omega}_a$ in the direction of $\hat{\mathbf{m}}_\mathbf{a}$ produces no change in the magnetic field applied to the capsule. As a result, the robot manipulator Jacobian $J_\mathcal{R}(\mathbf{q})$ can be converted into an actuator magnet Jacobian matrix $J_\mathcal{A}(\mathbf{q})$ that maps manipulator joint velocity $\dot{\mathbf{q}}$ to the actuator magnet's spatial velocity $\dot{\mathbf{p}}_\mathbf{a}$ and the actuator dipole moment's directional velocity $\dot{\hat{\mathbf{m}}}_\mathbf{a} = \boldsymbol{\omega}_\mathbf{a} \times \hat{\mathbf{m}}_\mathbf{a}$, with no contribution from the component of $\boldsymbol{\omega}_a$ parallel to $\hat{\mathbf{m}}_\mathbf{a}$, by

$$\begin{bmatrix} \dot{\mathbf{p}}_\mathbf{a} \\ \dot{\hat{\mathbf{m}}}_\mathbf{a} \end{bmatrix} = \begin{bmatrix} I & 0 \\ 0 & S(\hat{\mathbf{m}}_\mathbf{a})^\mathrm{T} \end{bmatrix} J_\mathcal{R}(\mathbf{q})\dot{\mathbf{q}} = J_\mathcal{A}(\mathbf{q})\dot{\mathbf{q}} \qquad (3)$$

where $S(\hat{\mathbf{m}}_\mathbf{a}) \in so(3)$ is the skew-symmetric form of the cross-product operation (see Appendix B). The matrix $J_\mathcal{A}(\mathbf{q})$ can be used to approximately map small changes in the manipulator's joints to small changes in actuator magnet position and small changes in the heading of the actuator magnet's dipole moment:

$$\begin{bmatrix} \delta\mathbf{p}_\mathbf{a} \\ \delta\hat{\mathbf{m}}_\mathbf{a} \end{bmatrix} \approx J_\mathcal{A}(\mathbf{q})\delta\mathbf{q} \qquad (4)$$

Note that $J_\mathcal{A}(\mathbf{q})$ is not invertible and is at most rank five, since the magnitude of $\hat{\mathbf{m}}_\mathbf{a}$ is constant by definition.

When the capsule is placed in the magnetic dipole field (1) generated by the actuator magnet, a magnetic torque $\boldsymbol{\tau}_\mathbf{m} = \mu_0\mathbf{m_c} \times \mathbf{h}(\mathbf{p}, \hat{\mathbf{m}}_\mathbf{a})$ and force $\mathbf{f}_\mathbf{m} = \mu_0(\mathbf{m_c} \cdot \nabla)\mathbf{h}(\mathbf{p}, \hat{\mathbf{m}}_\mathbf{a})$ are applied to the capsule's magnet, which are given by

$$\boldsymbol{\tau}_\mathbf{m}(\mathbf{p}, \hat{\mathbf{m}}_\mathbf{a}, \hat{\mathbf{m}}_\mathbf{c}) = \frac{\mu_0\|\mathbf{m_a}\|\|\mathbf{m_c}\|}{4\pi\|\mathbf{p}\|^3} \hat{\mathbf{m}}_\mathbf{c} \times D(\hat{\mathbf{p}})\hat{\mathbf{m}}_\mathbf{a} \qquad (5)$$

$$\mathbf{f}_\mathbf{m}(\mathbf{p}, \hat{\mathbf{m}}_\mathbf{a}, \hat{\mathbf{m}}_\mathbf{c}) = \frac{3\mu_0\|\mathbf{m_a}\|\|\mathbf{m_c}\|}{4\pi\|\mathbf{p}\|^4} \times$$
$$(\hat{\mathbf{m}}_\mathbf{a}\hat{\mathbf{m}}_\mathbf{c}^\mathrm{T} + \hat{\mathbf{m}}_\mathbf{c}\hat{\mathbf{m}}_\mathbf{a}^\mathrm{T} + (\hat{\mathbf{m}}_\mathbf{c}^\mathrm{T} Z\hat{\mathbf{m}}_\mathbf{a})I)\hat{\mathbf{p}} \qquad (6)$$

where $Z = I - 5\hat{\mathbf{p}}\hat{\mathbf{p}}^\mathrm{T}$ and $\mu_0 = 4\pi \times 10^{-7}$ N·A⁻² is the permeability of free-space. The magnetic torque aligns the capsule's dipole moment with the applied field, while the magnetic force pulls the capsule in a direction determined by the field's spatial derivatives and the capsule's dipole moment.

When the magnetic capsule is actuated in fluid at low speeds, small accelerations, and without contact with other objects, there is little resistance to change in the capsule's
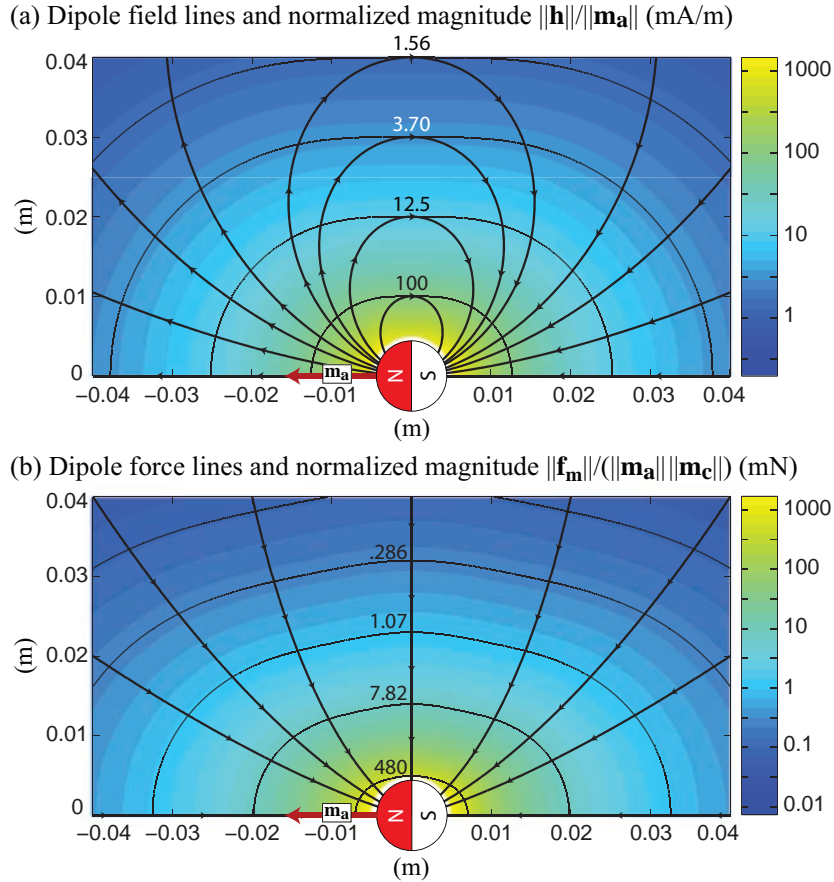
(a) Dipole field lines and normalized magnitude $\|\mathbf{h}\|/\|\mathbf{m_a}\|$ (mA/m)

(b) Dipole force lines and normalized magnitude $\|\mathbf{f_m}\|/(\|\mathbf{m_a}\|\|\mathbf{m_c}\|)$ (mN)

Fig. 1. Dipole field lines and the normalized actuator field magnitude $\|\mathbf{h}\|/\|\mathbf{m_a}\|$ are shown in (a). Magnetic force lines, generated with (6), assuming the capsule's moment $\mathbf{m_c}$ is aligned with the applied dipole field $\mathbf{h}$, and the resulting normalized magnetic force magnitude $\|\mathbf{f_m}\|/(\|\mathbf{m_a}\|\|\mathbf{m_c}\|)$, are shown in (b). When the capsule's dipole moment is aligned with the applied magnetic field, the magnetic force tends to be attractive. The color scale is logarithmic in both plots.

heading, which enables the magnetic torque to quickly align the capsule's dipole moment with the applied field. In these conditions, we can assume that the capsule's dipole moment is approximately aligned with the applied field for all time:

$$\hat{\mathbf{m}}_\mathbf{c}(\mathbf{p}, \hat{\mathbf{m}}_\mathbf{a}) \approx \hat{\mathbf{h}}(\mathbf{p}, \hat{\mathbf{m}}_\mathbf{a}) = D(\hat{\mathbf{p}})\hat{\mathbf{m}}_\mathbf{a} \qquad (7)$$

and the capsule's heading can be controlled by adjusting the direction of the magnetic field without controlling the magnetic torque directly using (5), which would require measurement of the direction of $\hat{\mathbf{m}}_\mathbf{c}$ (i.e. the capsule's heading). It also implies that $\hat{\mathbf{m}}_\mathbf{c}$ can be predicted by (7) using only a measurement of the position $\mathbf{p}$ obtained by a localization system, and that the magnetic force applied to the magnetic capsule can be predicted by substituting (7) into (6):

$$\mathbf{f_m}(\mathbf{p}, \hat{\mathbf{m}}_\mathbf{a}) \approx \frac{3\mu_0\|\mathbf{m_a}\|\|\mathbf{m_c}\|}{4\pi\|\mathbf{p}\|^4\|D(\hat{\mathbf{p}})\hat{\mathbf{m}}_\mathbf{a}\|}(\hat{\mathbf{m}}_\mathbf{a}\hat{\mathbf{m}}_\mathbf{a}^\mathrm{T} - (1 + 4(\hat{\mathbf{m}}_\mathbf{a}^\mathrm{T}\hat{\mathbf{p}})^2)I)\hat{\mathbf{p}}$$

$$(8)$$

Note that 5-DOF magnetic control can be performed without making the low-speed, small-acceleration, and non-

contact assumptions if a 5-DOF measurement of the capsule's pose (i.e. 3-DOF position and 2-DOF orientation of the capsule's dipole moment) is available. In this case, the applied magnetic force $\mathbf{f_m}$ and the direction of the applied magnetic torque $\hat{\boldsymbol{\tau}}_\mathbf{m}$ can be controlled independently (the torque magnitude cannot be controlled independently of the force magnitude). As we will demonstrate, 5-DOF control can still be achieved using only 3-DOF measurement of the capsule's position, provided the capsule is free to align itself with the applied field.

The total force $\mathbf{f}$ applied to the capsule consists of the apparent weight $\mathbf{f_w}$ (sum of the capsule's weight and buoyant force), which is constant, and the magnetic force $\mathbf{f_m}$. We assume that the capsule is heavier than its buoyant force, making $\mathbf{f_w}$ point in the direction of gravity. In this case, the capsule can be made to levitate by positioning the actuator magnet above the capsule where the attractive magnetic force perfectly balances the capsule's apparent weight and the magnitude of the total applied force $\mathbf{f}$ is zero. If the capsule is desired to ascend, then the actuator magnet is moved closer so that the magnetic force is larger than the capsule's apparent weight and the total applied

force is directed upward. If the capsule is desired to descend, then the actuator magnet is positioned farther away from the capsule's levitation position and the total applied force points down. The maximum downward force that can be applied is the capsule's apparent weight $\mathbf{f_w}$.

Using (7) and (8), a nonlinear magnetic actuation equation can be formed that relates the relative position $\mathbf{p}$ and the direction of the actuator magnet $\hat{\mathbf{m}}_\mathbf{a}$ to the total applied force $\mathbf{f}$ and the direction of the applied magnetic field $\hat{\mathbf{h}}$:

$$\begin{bmatrix} \mathbf{f} \\ \hat{\mathbf{h}} \end{bmatrix} = \begin{bmatrix} \mathbf{f_m}(\mathbf{p}, \hat{\mathbf{m}}_\mathbf{a}) + \mathbf{f_w} \\ \widehat{D(\hat{\mathbf{p}})\hat{\mathbf{m}}_\mathbf{a}} \end{bmatrix} = \mathcal{F}(\mathbf{p}, \hat{\mathbf{m}}_\mathbf{a}) \qquad (9)$$

which is purely a function of the actuator magnet's pose, that is, the relative position $\mathbf{p}$ and the actuator magnet's dipole moment direction $\hat{\mathbf{m}}_\mathbf{a}$, which in turn are purely specified by the capsule's position $\mathbf{p_c}$ and the robot manipulator's pose $\mathbf{q}$.

In order to solve the inverse problem (i.e. computing the necessary manipulator pose that will apply a desired total applied force and applied magnetic field heading, given the capsule's position), the nonlinear actuation equation (9) is first linearized with the Jacobian matrix $J_\mathcal{F}(\mathbf{p}, \hat{\mathbf{m}}_\mathbf{a}) \in \mathbb{R}^{6 \times 6}$, computed by differentiating (9) with respect to the relative position $\mathbf{p}$ and the actuator dipole moment $\hat{\mathbf{m}}_\mathbf{a}$. (The components of $J_\mathcal{F}(\mathbf{p}, \hat{\mathbf{m}}_\mathbf{a})$ are defined in Appendix C.) Linearization produces the approximate mapping between small changes in relative position and actuator-moment direction to small changes in the applied force and field heading:

$$\begin{bmatrix} \delta \mathbf{f} \\ \delta \hat{\mathbf{h}} \end{bmatrix} \approx J_\mathcal{F}(\mathbf{p}, \hat{\mathbf{m}}_\mathbf{a}) \begin{bmatrix} \delta \mathbf{p} \\ \delta \hat{\mathbf{m}}_\mathbf{a} \end{bmatrix} \qquad (10)$$

$$= J_\mathcal{F}(\mathbf{p}, \hat{\mathbf{m}}_\mathbf{a}) \left(\begin{bmatrix} \delta \mathbf{p_c} \\ \mathbf{0} \end{bmatrix} + \begin{bmatrix} -I & 0 \\ 0 & I \end{bmatrix} \begin{bmatrix} \delta \mathbf{p_a} \\ \delta \hat{\mathbf{m}}_\mathbf{a} \end{bmatrix} \right) \qquad (11)$$

where (11) results from substituting $\delta \mathbf{p} = \delta \mathbf{p_c} - \delta \mathbf{p_a}$ into (10). The relation (11) divides a small change in applied total force and applied field heading into the result of a small change in capsule position $\delta \mathbf{p_c}$ and a small change in the actuator magnet's pose (i.e. in the actuator magnet position $\delta \mathbf{p_a}$ and dipole heading $\delta \hat{\mathbf{m}}_\mathbf{a}$), which is related to small changes in the manipulator's joints by the Jacobian $J_\mathcal{A}(\mathbf{q})$, given by (4).

Substituting (4) into (11) produces the relationship between small changes in the manipulator's joints and capsule position and small changes in applied total force and field heading:

$$\begin{bmatrix} \delta \mathbf{f} \\ \delta \hat{\mathbf{h}} \end{bmatrix} \approx J_{\mathcal{F}\mathcal{A}}(\mathbf{p}, \mathbf{q}) \delta \mathbf{q} + J_\mathcal{F}(\mathbf{p}, \hat{\mathbf{m}}_\mathbf{a}) \begin{bmatrix} \delta \mathbf{p_c} \\ \mathbf{0} \end{bmatrix} \qquad (12)$$

$$J_{\mathcal{F}\mathcal{A}}(\mathbf{p}, \mathbf{q}) = J_\mathcal{F}(\mathbf{p}, \hat{\mathbf{m}}_\mathbf{a}) \begin{bmatrix} -I & 0 \\ 0 & I \end{bmatrix} J_\mathcal{A}(\mathbf{q}) \qquad (13)$$

The actuator magnet's dipole moment $\hat{\mathbf{m}}_\mathbf{a}$ does not appear in the arguments of $J_{\mathcal{F}\mathcal{A}}$ since $\hat{\mathbf{m}}_\mathbf{a}$ is set by the robot

manipulator's joints $\mathbf{q}$ using the manipulator's forward kinematics.

Equation (12) is intended to be used inside a control loop where small changes in capsule position $\delta \mathbf{p_c}$ are obtained by a capsule localization system, and $\delta \mathbf{f}$ and $\delta \hat{\mathbf{h}}$ are small desired changes produced by a controller governing the magnetic capsule's pose. In this context, the terms of (12) can be rearranged to produce

$$\delta \mathbf{d} \equiv \begin{bmatrix} \delta \mathbf{f} \\ \delta \hat{\mathbf{h}} \end{bmatrix} - J_\mathcal{F}(\mathbf{p}, \hat{\mathbf{m}}_\mathbf{a}) \begin{bmatrix} \delta \mathbf{p_c} \\ \mathbf{0} \end{bmatrix} \approx J_{\mathcal{F}\mathcal{A}}(\mathbf{p}, \mathbf{q}) \delta \mathbf{q} \qquad (14)$$

where $\delta \mathbf{d}$ is a desired change in applied force and field heading resulting *only* from a change in the manipulator's joints. Equation (14) can be inverted to produce the inverse mapping of desired change in applied force and a change in field heading to a necessary change in the manipulator's joints using the Moore–Penrose pseudoinverse:

$$\delta \mathbf{q} \approx J_{\mathcal{F}\mathcal{A}}(\mathbf{p}, \mathbf{q})^\dagger \delta \mathbf{d} \qquad (15)$$

If multiple solutions of (15) are possible (i.e. the manipulator has more than five DOFs), then the pseudoinverse solves (15) and minimizes $\|\delta \mathbf{q}\|$ (a generalized pseudoinverse can be applied for a manipulator where the units of $\delta \mathbf{q}$ are inconsistent; Doty et al., 1993). Given an initial joint configuration $\mathbf{q}_0$, (15) can be integrated in time to produce $\mathbf{q}_t$ without explicitly solving the inverse kinematics of the complete manipulator–magnet system (Sciavicco and Siciliano, 2000). This approach breaks down when the manipulator is near a kinematic singularity, which we will address later in this paper.

2.1. Analyzing the Jacobian $J_{\mathcal{F}\mathcal{A}}(\mathbf{p}, \mathbf{q})$

For 5-DOF holonomic control, $J_{\mathcal{F}\mathcal{A}}(\mathbf{p}, \mathbf{q})$ must be rank five. Since $J_{\mathcal{F}\mathcal{A}}(\mathbf{p}, \mathbf{q})$ is the product of $J_\mathcal{F}(\mathbf{p}, \hat{\mathbf{m}}_\mathbf{a})$ and $J_\mathcal{A}(\mathbf{q})$, we will analyze the rank of the Jacobian $J_\mathcal{F}(\mathbf{p}, \hat{\mathbf{m}}_\mathbf{a})$ and the Jacobian $J_\mathcal{A}(\mathbf{q})$ separately. For readability, we will refer to the Jacobians $J_{\mathcal{F}\mathcal{A}}(\mathbf{p}, \mathbf{q})$, $J_\mathcal{F}(\mathbf{p}, \hat{\mathbf{m}}_\mathbf{a})$ and $J_\mathcal{A}(\mathbf{q})$ without their arguments in the text (i.e. as $J_{\mathcal{F}\mathcal{A}}$, $J_\mathcal{F}$, and $J_\mathcal{A}$).

Prior to analyzing the rank of $J_\mathcal{F}$, we first scale the columns and rows of $J_\mathcal{F}$ to produce a nondimensional Jacobian $\tilde{J}_\mathcal{F}$ that approximately maps its pre-image, consisting of nondimensional changes in position $\delta \mathbf{p}/\|\mathbf{p}\|$ and changes in actuator magnet heading $\delta \hat{\mathbf{m}}_\mathbf{a}$ (already nondimensional), to its image, consisting of nondimensional changes in force $\delta \mathbf{f}/\|\mathbf{f_m}\|$ and applied field heading $\delta \hat{\mathbf{h}}$ (already nondimensional):

$$\tilde{J}_\mathcal{F}(\mathbf{p}, \hat{\mathbf{m}}_\mathbf{a}) = \begin{bmatrix} \frac{1}{\|\mathbf{f_m}\|}I & 0 \\ 0 & I \end{bmatrix} J_\mathcal{F} \begin{bmatrix} \|\mathbf{p}\|I & 0 \\ 0 & I \end{bmatrix} \qquad (16)$$

where $I \in \mathbb{R}^{3 \times 3}$ is the identity matrix (scaling by $\|\mathbf{f_m}\|^{-1}$ is safe since $\|\mathbf{f_m}\| \neq 0$ when $\hat{\mathbf{m}}_\mathbf{c} \approx \hat{\mathbf{h}}$).

The nondimensional Jacobian $\tilde{J}_\mathcal{F}$ is produced by post- and premultiplying $J_\mathcal{F}$ with a series of elementary matrices, which guarantees that rank $\tilde{J}_\mathcal{F}$ = rank $J_\mathcal{F}$ and enables the

rank of $J_\mathcal{F}$ to be found using the singular value decomposition of $\tilde{J}_\mathcal{F}$ with unit-consistent singular values, which reveal the rank of $J_\mathcal{F}$. Since the applied field direction $\hat{\mathbf{h}}$ cannot change in a direction parallel to itself, the smallest singular value σ_6 must be zero. The second smallest singular value σ_5 reveals whether rank $\tilde{J}_\mathcal{F} = 5$. Figure 2 shows σ_5 plotted on a plane in which the actuator dipole moment $\mathbf{m_a}$ lies. Because the magnetic field is radially symmetric about the dipole moment $\mathbf{m_a}$, a plot of σ_5 on any plane in which $\mathbf{m_a}$ lies will be equivalent to Figure 2. The minimum value taken on by σ_5 is 0.123, indicating that $\tilde{J}_\mathcal{F}$ (and thus $J_\mathcal{F}$) is always rank five.

The fact that $J_\mathcal{F}$ is always rank five implies that a single permanent magnet in space, irrespective of the robot manipulator that maneuvers it, can exhibit 5-DOF control over an untethered magnetic device. The ability of a complete robotic system, including magnet and manipulator, to exhibit 5-DOF magnetic control is precluded only by the ability of the robot manipulator to position the actuator magnet with three DOFs and the actuator magnet's dipole moment with two DOFs. If the rank of the Jacobian $J_\mathcal{A}$ is five, then the robotic system possesses 5-DOF control over the untethered capsule. If the actuator magnet pose required to achieve a desired applied total force and magnetic field heading places the manipulator into a kinematic singularity, then 5-DOF magnetic control is lost.

We numerically analyze the configurations of total forces and field headings that make the manipulator enter a singularity by first nondimensionalizing the Jacobian $J_\mathcal{A}$ as

$$\tilde{J}_\mathcal{A}(\mathbf{q}) = \begin{bmatrix} \frac{1}{\|\mathbf{p}\|}I & 0 \\ 0 & I \end{bmatrix} J_\mathcal{A}(\mathbf{q}) \tag{17}$$

which can then be substituted, along with $\tilde{J}_\mathcal{F}$, into (13) for $J_\mathcal{F}$ and $J_\mathcal{A}$ to produce the normalized Jacobian

$$\tilde{J}_{\mathcal{F}\mathcal{A}}(\mathbf{p},\mathbf{q}) = \tilde{J}_\mathcal{F}(\mathbf{p},\hat{\mathbf{m}}_\mathbf{a}) \begin{bmatrix} -I & 0 \\ 0 & I \end{bmatrix} \tilde{J}_\mathcal{A},(\mathbf{q}) \tag{18}$$
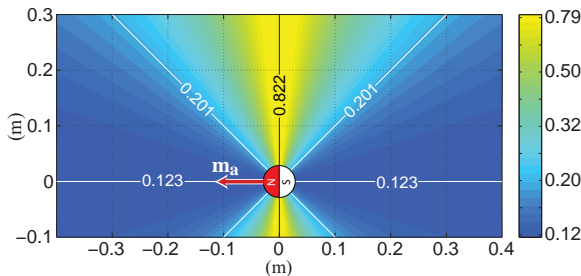

Fig. 2. The second smallest singular value, σ_5, of the normalized magnetic actuation Jacobian $\tilde{J}_F$ is plotted (with a logarithmic color scale) on any plane in which the actuator dipole moment $\mathbf{m_a}$ lies. The smallest value taken on by σ_5 is 0.123 and occurs on the line on which the dipole $\mathbf{m_a}$ lies. The fact that $\sigma_5 > 0$ indicates that $\tilde{J}_F$ (and thus J_F) is always rank five.

which approximately maps change in manipulator joints $\delta\mathbf{q}$ (already nondimensional) to change in nondimensional applied force and change in field heading (already nondimensional).

The Moore–Penrose pseudoinverse $\tilde{J}_{\mathcal{F}\mathcal{A}}^{\dagger}$ is the inverse mapping that minimizes $\|\delta\mathbf{q}\|$ if the robot manipulator is over-actuated. The largest singular value of $\tilde{J}_{\mathcal{F}\mathcal{A}}^{\dagger}$ (i.e. the reciprocal of the smallest non-zero singular value of $\tilde{J}_{\mathcal{F}\mathcal{A}}$) can be used to describe the worst case of how a unit-magnitude vector of nondimensional change in applied force and field heading are approximately mapped to a magnitude change in manipulator joints. If the largest singular value approaches infinity, then the robot manipulator is near a kinematic singularity.

As an example, consider the case where a magnetic capsule is desired to point downward (in the direction of gravity) as it is being repositioned by an applied magnetic force, and the robotic manipulator used to maneuver the actuator magnet is a 6-DOF serial link manipulator. For this example, we have assumed the magnetic capsule, actuator magnet, and robotic manipulator are those used for the experiments herein and the capsule is placed in a typical position in front of the manipulator as illustrated in Figure 3. In Figure 3(a) and (b), the manipulator's workspace has been sliced into $\hat{\mathbf{x}},\hat{\mathbf{z}}$ and $\hat{\mathbf{y}},\hat{\mathbf{z}}$ planes. For every possible actuator magnet position on both planes, the actuator magnet's dipole direction $\hat{\mathbf{m}}_\mathbf{a}$ is set to guarantee that the applied field at the capsule position points in the $-\hat{\mathbf{z}}$ direction. The necessary heading of the actuator magnet's dipole moment $\hat{\mathbf{m}}_\mathbf{a}$ is given by

$$\hat{\mathbf{m}}_\mathbf{a} = -\widehat{D^{-1}(\hat{\mathbf{p}})}\hat{\mathbf{z}} \tag{19}$$

where $D^{-1}(\hat{\mathbf{p}}) = (D(\hat{\mathbf{p}}) - I)/2$ admits a unique actuator magnet pose for every actuator magnet position (Mahoney and Abbott, 2014b).

The largest singular values of $\tilde{J}_{\mathcal{F}\mathcal{A}}^{\dagger}$ resulting from the robot manipulator configuration that places the actuator magnet in every feasible position in the $\hat{\mathbf{x}},\hat{\mathbf{z}}$ and $\hat{\mathbf{y}},\hat{\mathbf{z}}$ planes and directs the actuator magnet's moment according to (19) are shown in Figure 3(a) and (b). The regions where the manipulator nears its spherical-wrist kinematic singularity cause the singular value to become large. The regions outside the manipulator's reachable workspace are shown in gray.

Each actuator magnet pose causes a magnetic force to be applied to the capsule. Fifteen numbered actuator magnet poses are illustrated in Figure 3(a) and (b) along with the resulting correspondingly numbered total force vectors applied to the capsule. Each force vector denotes a total force magnitude of $\|\mathbf{f}\| = 0.3$ mN. The resulting manipulator poses for select numbered total force vectors are shown in Figure 3(c). The pose that balances the applied magnetic force and the capsule's apparent weight is labeled as pose '0'. The manipulator's physical workspace limits and kinematic singularities complicate which forces the system can apply. For example, due to workspace limits of the
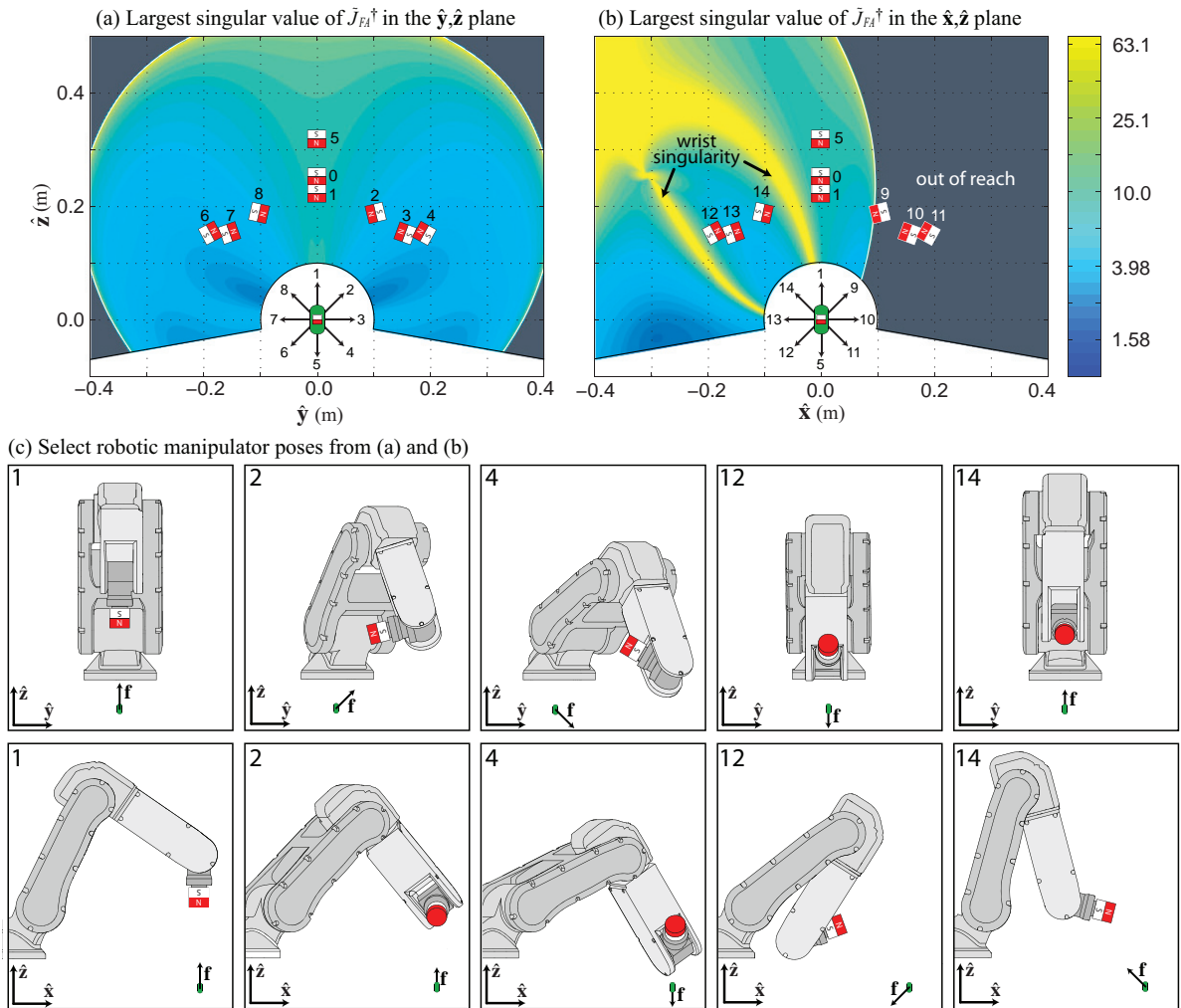
Fig. 3. The largest singular value of the nondimensional Jacobian $\tilde{J}_{FA}{}^\dagger$ is shown in (a) the $\hat{\mathbf{y}}, \hat{\mathbf{z}}$ plane and in (b) the $\hat{\mathbf{x}}, \hat{\mathbf{z}}$ plane, plotted in a logarithmic color scale, for a scenario where a capsule (positioned as shown) is desired to point downward ($\hat{\mathbf{m}}_c = -\hat{\mathbf{z}}$). The singular value plots are generated by placing the actuator magnet at every position in the $\hat{\mathbf{y}}, \hat{\mathbf{z}}$ and $\hat{\mathbf{x}}, \hat{\mathbf{z}}$ planes and directing the actuator magnet's dipole moment $\mathbf{m}_a$ so that the applied field at the capsule's position points the capsule down. The regions outside the reachable workspace of the manipulator are shown in gray. The regions where the largest singular value exceeds approximately 70 correspond to an actuator magnet pose that places the manipulator near a kinematic singularity. Fifteen numbered actuator poses are shown in (a) and (b) that correspond to the application of a correspondingly numbered 0.3 mN total force acting on the capsule depicted in the figure. Pose '0' is the equilibrium position where the net applied force is zero. Select manipulator configurations for five of the 15 poses are shown in (c).

manipulator, forces labeled '9', '10', and '11' are not achievable, and due to the manipulator's wrist singularity, transitions from the capsule levitation configuration (pose '0') to a 0.3 mN force in the $-\hat{\mathbf{x}}$ direction (pose '13') would require the manipulator to pass through its wrist singularity. Note that the direction of the actuator magnet's dipole moment satisfies (19) and applies a magnetic field in the $-\hat{\mathbf{z}}$ direction at the capsule's position.

Figure 4(a) and (b) shows the largest singular value of $\tilde{J}_{FA}{}^\dagger$ where the actuator magnet is oriented to direct the capsule in the $-\hat{\mathbf{x}}$ direction (i.e. $\hat{\mathbf{m}}_c = -\hat{\mathbf{x}}$). Fifteen actuator magnet poses that achieve the same 15 applied 0.3 mN numbered forces as Figure 3 are shown in Figure 4(a) and (b), with the robot manipulator pose for select applied

forces shown in Figure 4(c). Requiring that the capsule point in the $-\hat{\mathbf{x}}$ direction changes the necessary actuator magnet pose to achieve the same applied forces as in Figure 3. In this case, the actuator magnet must be oriented so that the capsule is positioned in the region of the actuator magnet's dipole field where the applied magnetic force magnitude is weakest (see Figure 1) and the actuator must be positioned closer to the capsule. For example, to maintain the capsule at equilibrium (pose '0') the actuator must be positioned a distance of 212 mm above the capsule when $\hat{\mathbf{m}}_c = -\hat{\mathbf{x}}$, compared to a distance of 252 mm when $\hat{\mathbf{m}}_c = -\hat{\mathbf{z}}$.

Note that mounting the actuator magnet to the robot arm so that the actuator magnet's dipole moment is parallel
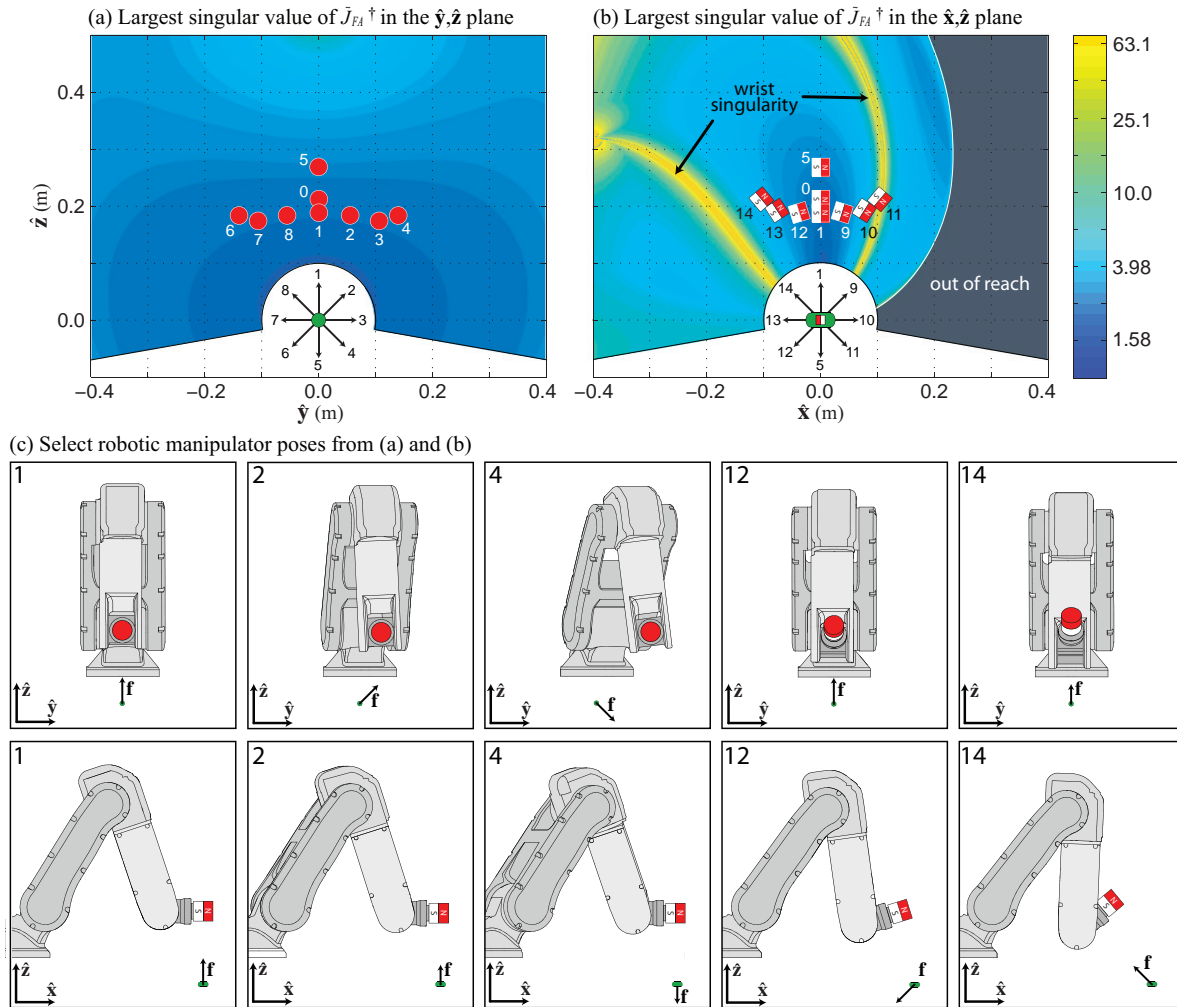
Fig. 4. The largest singular value of the nondimensional Jacobian $\tilde{J}_{FA}{}^{\dagger}$ is shown in (a) the $\hat{\mathbf{y}}, \hat{\mathbf{z}}$ plane and in (b) the $\hat{\mathbf{x}}, \hat{\mathbf{z}}$ plane, plotted in a logarithmic color scale, for a scenario where a capsule (positioned as shown) is desired to be horizontal ($\hat{\mathbf{m}}_c = -\hat{\mathbf{x}}$). The singular value plots are generated by placing the actuator magnet at every position in the $\hat{\mathbf{y}}, \hat{\mathbf{z}}$ and $\hat{\mathbf{x}}, \hat{\mathbf{z}}$ planes and directing the actuator magnet's dipole moment $\mathbf{m_a}$ so that the applied field at the capsule's position points the capsule so that $\hat{\mathbf{m}}_c = -\hat{\mathbf{x}}$. The regions outside the reachable workspace of the manipulator are shown in gray. The regions where the largest singular value exceeds approximately 70 correspond to an actuator magnet pose that place the manipulator near a kinematic singularity. Fifteen numbered actuator poses are shown in (a) and (b) that correspond to the application of a correspondingly numbered 0.3 mN total force acting on the capsule depicted in the figure. Pose '0' is the equilibrium position where the net applied force is zero. Select manipulator configurations for five of the 15 poses are shown in (c).

to the axis of the manipulator's most distal joint (as shown in Figures 3(c) and 4(c)) effectively reduces the 6-DOF kinematic chain of the manipulator to five DOFs, which results in the manipulator's kinematic singularities exhibiting themselves as singularities of the complete system (as shown in Figures 3(a) and 4(a)). Increasing the robot manipulator's kinematic DOFs beyond five by adding more DOFs (or mounting the actuator magnet so that its dipole moment is perpendicular to the axis of the most distal joint, in the case of the robot manipulator used herein) creates a system that is kinematically over-actuated, to which classical robotics methods can be applied (Sciavicco and Siciliano, 2000). However, if the system is not kinematically over-actuated, then singularities must be dealt with.

2.2. Managing manipulator singularities

Managing the joint motion of a robot manipulator near kinematic singularities while applying differential kinematic inversion is well-studied (Sciavicco and Siciliano, 2000). A common approach is the method of damped least-squares, which minimizes a cost function containing competing terms that penalize tracking error in the end-effector configuration and that penalize the magnitude of joint motion (Wampler, 1986; Chiaverini et al., 1994). Damped least-squares methods sacrifice tracking performance to reduce joint motion near kinematic singularities.

In the context of magnetic manipulation, tracking error in the actuator magnet's configuration will cause error in the desired magnetic force and field heading applied to the

capsule, potentially resulting in loss of control. Rather than potentially sacrificing total capsule control when the manipulator nears a singularity, we have chosen to implement a strategy that sacrifices control over the capsule's heading while maintaining control over the magnetic force applied to the capsule. When the actuator magnet is positioned by a robot manipulator with at least five DOFs, sacrificing heading control effectively transforms the total magnetic manipulation system into one that is kinematically over-actuated. In the context of stomach capsule endoscopy, temporarily sacrificing precise control over the capsule's heading may not preclude visualization since existing capsule endoscopes have large fields of view. For example, Given Imaging's commercially available PillCam$^{\text{TM}}$ SB2 has a 156° field of view (Valdastri et al., 2012b).

Given some small desired change in applied field heading $\delta\hat{\mathbf{h}}_{\mathbf{d}}$ and some small desired change in applied magnetic force $\delta\mathbf{f}_{\mathbf{d}}$, the problem of sacrificing heading control while maintaining control over the applied magnetic force is posed as a constrained, quadratic least-squares problem:

$$\underset{\delta\mathbf{q}}{\text{minimize}} \quad \left\| \frac{\partial\hat{\mathbf{h}}}{\partial\mathbf{q}}\delta\mathbf{q} - \delta\hat{\mathbf{h}}_{\mathbf{d}} \right\|^2 \tag{20}$$

$$\text{subject to} \quad \frac{\partial\mathbf{f}}{\partial\mathbf{q}}\delta\mathbf{q} = \delta\mathbf{f}_{\mathbf{d}} \tag{21}$$

$$\|W\delta\mathbf{q}\| \le r \tag{22}$$

where the matrices $\partial\mathbf{f}/\partial\mathbf{q} \in \mathbb{R}^{3\times n}$ and $\partial\hat{\mathbf{h}}/\partial\mathbf{q} \in \mathbb{R}^{3\times n}$ are the top and bottom three rows of the Jacobian $J_{\mathcal{F}\mathcal{A}}$, respectively. The constraint (21) guarantees the desired change in applied force $\delta\mathbf{f}_{\mathbf{d}}$ is met (provided $\partial\mathbf{f}/\partial\mathbf{q}$ has full row rank), and the constraint (22) enforces a maximum bound on the magnitude of joint motion weighted by the invertible matrix W. The cost function (20) attempts to reduce the error between the desired and actual change in applied field heading. The weight matrix W can be used to increase the 'cost' of select joint motions or to homogenize disparate units of $\delta\mathbf{q}$.

The formulation can be rewritten in compact notation as

$$\underset{\mathbf{v}}{\text{minimize}} \quad \|A\mathbf{v} - \mathbf{b}\|^2 \tag{23}$$

$$\text{subject to} \quad B\mathbf{v} = \mathbf{c} \tag{24}$$

$$\|\mathbf{v}\| \le r \tag{25}$$

where $\mathbf{v} = W\delta\mathbf{q}$, $\mathbf{b} = \delta\hat{\mathbf{h}}_{\mathbf{d}}$, $\mathbf{c} = \delta\mathbf{f}_{\mathbf{d}}$, $A = (\partial\hat{\mathbf{h}}/\partial\mathbf{q})W^{-1}$, and $B = (\partial\mathbf{f}/\partial\mathbf{q})W^{-1}$.

If desired, the formulation (23) to (25) can be used inside an iterative method to solve the combined inverse kinematics of the actuator magnet and robot manipulator. Such methods have been used in the general application of constrained optimization, where they are referred to as 'trust-region' iteration methods due to the ability of the constraint (25) to limit every iterative step to a region where the underlying model is 'trusted'. In the case of our

formulation, the constraint (25) would keep the result of each iteration within a region where A and B (which are results of linearization) are accurate. The implementation of the controller used herein does not take an iterative approach; rather, the formulation (23) to (25) is solved at each controller time-step. This simultaneously keeps $\delta\mathbf{q}$ within a region where the linearizations A and B are accurate and limits the motion of the robot manipulator.

There are two ways for the formulation (23) to (25) to break down. The first is if the matrix B does not have full row rank and the constraint (24) is not satisfiable. In the context of magnetic manipulation this could occur if $\partial\mathbf{f}/\partial\mathbf{q}$ loses full row rank in certain manipulator-dependent configurations (an example for the 6-DOF robotic manipulator used for the experiments herein is described later). The second is if the equality (24) and quadratic (25) constraints become mutually exclusive, which could occur if $\|\mathbf{c}\|$ is large or B becomes ill-conditioned, resulting in large magnitude solutions for $\mathbf{v}$ to satisfy the constraint (24). In the context of magnetic manipulation, this could occur if the desired change in applied force $\delta\mathbf{f}_{\mathbf{d}}$ is too large for the given bound on joint motion r or $\partial\mathbf{f}/\partial\mathbf{q}$ becomes ill-conditioned. These conditions will be discussed in the text that follows.

We present a solution in the context of our application that solves the optimization problem by first eliminating the equality constraint (24) and then ensuring that the result satisfies the quadratic constraint (25). Assuming the matrix B has full row rank and the robot manipulator has at least five DOFs, the nullspace of B (i.e. null(B)) is guaranteed to have dimension of at least two. The solution $\mathbf{v}^*$ that minimizes (23) and satisfies the constraints is composed of the sum of a component lying purely in the column space of B that satisfies the equality constraint (24), and an orthogonal component lying in null(B) that minimizes (23), taking the form

$$\mathbf{v}^* = B^{\dagger}\mathbf{c} + N\mathbf{k} \tag{26}$$

where $B^{\dagger}$ is the Moore–Penrose pseudoinverse of B, and N is the orthonormal matrix whose columns span null(B). The solution $\mathbf{v}^*$ can be interpreted as the sum of a term that satisfies the equality constraint (i.e. the left term) and a term that attempts to minimizer the error of the desired quantity created by satisfying the equality constraint (i.e. the right term). This solution is frequently used in the inverse kinematics of redundant manipulators (Sciavicco and Siciliano, 2000).

The vector $\mathbf{k}$ that minimizes the cost function (23) and satisfies the quadratic constraint (25) must be found. Because the terms of $\mathbf{v}^*$ are perpendicular and N is orthonormal, applying the quadratic constraint (25) to $\mathbf{v}^*$ produces

$$\|\mathbf{v}^*\|^2 = \left\|B^{\dagger}\mathbf{c}\right\|^2 + \|N\mathbf{k}\|^2 = \left\|B^{\dagger}\mathbf{c}\right\|^2 + \|\mathbf{k}\|^2 \le r^2 \tag{27}$$

which yields the maximum bound on $\|\mathbf{k}\|^2$ that guarantees the quadratic constraint (25) is satisfied:

$$\|\mathbf{k}\|^2 \le r^2 - \left\|B^\dagger \mathbf{c}\right\|^2 \qquad (28)$$

If $r^2 - \|B^\dagger \mathbf{c}\|^2 < 0$, then the equality constraint (24) and the constraint (25) are mutually exclusive, making no solution possible unless r is increased. This can occur if $\|\mathbf{c}\|$ is large or B is poorly conditioned.

Otherwise, substituting $\mathbf{v}^*$ for $\mathbf{v}$ in (23) ensures the equality constraint (24) is satisfied and produces a new, feasible minimization problem in terms of the vector $\mathbf{k}$:

$$\underset{\mathbf{k}}{\text{minimize}} \quad \left\|AN\mathbf{k} + AB^\dagger \mathbf{c} - \mathbf{b}\right\|^2 \qquad (29)$$

$$\text{subject to} \quad \|\mathbf{k}\|^2 \le r^2 - \left\|B^\dagger \mathbf{c}\right\|^2 \qquad (30)$$

The solution $\mathbf{k}^*$ that minimizes (29), without necessarily satisfying the quadratic constraint (30), can be found using the Moore–Penrose pseudoinverse as

$$\mathbf{k}^* = (AN)^\dagger \left(\mathbf{b} - AB^\dagger \mathbf{c}\right) \qquad (31)$$

If $\mathbf{k}^*$ satisfies the quadratic constraint (30) then $\mathbf{k}^*$ can be immediately substituted into (26) for $\mathbf{k}$ to produce

$$\mathbf{v}^* = B^\dagger \mathbf{c} + N(AN)^\dagger \left(\mathbf{b} - AB^\dagger \mathbf{c}\right) \qquad (32)$$

which solves the formulation (23) to (25). The joint-angle solution $\delta\mathbf{q}^*$ that solves the formulation (20) to (22) can then be found as $\delta\mathbf{q}^* = W^{-1}\mathbf{v}^*$. In this case, the quadratic constraint (30) is inactive and does not influence the result of $\mathbf{v}^*$. If the Jacobian $J_{\mathcal{FA}}$ is rank-five (i.e. the robot manipulator is not near a singularity), then the joint solution $\delta\mathbf{q}^*$ is equivalent to that found with the pseudoinverse as in (15).

If (31) does not satisfy the quadratic constraint (30), then the method of 'complete diagonalization' can be applied to find a $\mathbf{k}^*$ such that quadratic constraint (30) is satisfied via equality. The process of complete diagonalization requires the eigen-decomposition of the matrix AN and either a numerical solution for the roots of a function for which bounds are known, or the solution for the roots of a polynomial (of at least degree four) using the eigenvalues of a corresponding companion matrix. A complete description of the method can be found in Hager (2001). The solution $\mathbf{k}^*$ resulting from complete diagonalization can then be substituted into (26) to produce $\mathbf{v}^*$. Once $\mathbf{v}^*$ has been found, the change in joint angles that solve the formulation (20) to (22) is found as $\delta\mathbf{q}^* = W^{-1}\mathbf{v}^*$.

The scenario when the matrix B becomes ill-conditioned (or loses full row rank) can cause the constraints of the formulation (23) to (25) to become unsatisfiable. Although when (or if) this can occur depends solely on the kinematics of the robot manipulator, properties of the actuator's dipole field can exacerbate issues, particularly if the robot manipulator contains a spherical wrist. Consider an actuator–capsule configuration shown in Figure 5, where the actuator

and capsule dipole moments are parallel (but in opposite directions) and the relative position is perpendicular to both dipole moments. In this configuration the top three rows of the nondimensional magnetic dipole Jacobian $\tilde{J}_{\mathcal{F}}$, given by (16), approximately relate small, nondimensional changes in relative position $\delta\mathbf{p}/\|\mathbf{p}\|$ and actuator moment direction $\delta\hat{\mathbf{m}}_\mathbf{a}$ to small, nondimensional changes in applied magnetic force $\delta\mathbf{f}_\mathbf{m}/\|\mathbf{f}_\mathbf{m}\|$, taking the form

$$\frac{\delta\mathbf{f}_\mathbf{m}}{\|\mathbf{f}_\mathbf{m}\|} \approx \begin{bmatrix} 0 & 0 & 0 & 0 & 0 & -1 \\ 0 & -1 & 0 & 0 & 0 & 0 \\ 0 & 0 & 4 & 0 & 0 & 0 \end{bmatrix} \begin{bmatrix} \frac{\delta\mathbf{p}}{\|\mathbf{p}\|} \\ \delta\hat{\mathbf{m}}_\mathbf{a} \end{bmatrix} \qquad (33)$$

In this example, it is clear that the top three rows of $\tilde{J}_{\mathcal{F}}$ have full row rank and any small change in applied magnetic force is possible with some change in relative position or actuator dipole moment. In this configuration, however, the necessary changes in relative position and actuator moment are particularly nonintuitive. Equation (33) shows that small changes in $\delta\mathbf{p}$ in the $\hat{\mathbf{x}}$ direction produce no change in the applied magnetic force in the $\hat{\mathbf{x}}$ direction. Instead, change in applied magnetic force in the $\pm\hat{\mathbf{x}}$ direction requires rotating the actuator moment around the $\pm\hat{\mathbf{y}}$ axis, a motion that could be infeasible if the manipulator's wrist is at or near its singularity. This case is illustrated in Figure 5, which shows the manipulator used in the experiments with wrist axes $\hat{\mathbf{a}}_3$, $\hat{\mathbf{a}}_4$, and $\hat{\mathbf{a}}_5$, placed in a configuration where the wrist kinematics have become singular ($\hat{\mathbf{a}}_3$ and $\hat{\mathbf{a}}_5$ are parallel). In this example, magnetic force in the $\pm\hat{\mathbf{x}}$ direction cannot be controlled due to the manipulator's kinematic singularity, and the B matrix would not have full row rank in the formulation (23) to (25).

Systems should be designed to make configurations of the form described in the preceding example impossible or highly unlikely either by design, or by actively preventing a user (e.g. clinician) from controlling the capsule in a manner that would cause the system to enter such a configuration. One potential approach toward this end could be to prevent the user from controlling the capsule into a configuration where the metric

$$w = \sqrt{\det(BB^\mathrm{T})} \qquad (34)$$

which decreases as B loses row rank, passes below a predefined threshold. If this occurs, user inputs that cause w to decrease (i.e. $\delta w \le 0$) should be rejected.

2.3. Scaling the actuator magnet

The fact that the applied magnetic force (6) rapidly increases as $\|\mathbf{p}\|$ decreases implies that any variation in the actual applied magnetic force caused by error in the estimated capsule position will be large when the capsule is actuated close to the actuator magnet. The separation distance when the capsule is in equilibrium is a function of the capsule's apparent weight $\|\mathbf{f}_\mathbf{w}\|$ and the product of the actuator and capsule dipole moment magnitudes $\|\mathbf{m}_\mathbf{a}\|\|\mathbf{m}_\mathbf{c}\|$,
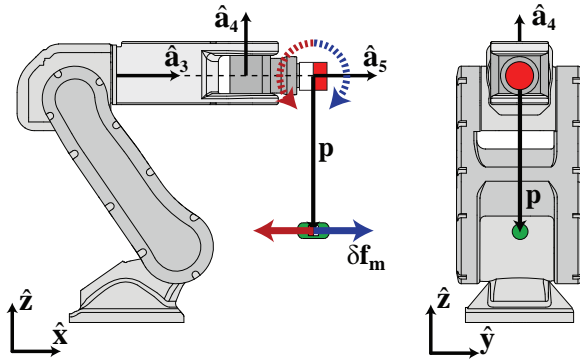
Fig. 5. A scenario when the matrix *B* can lose full rank and the constraints of the formulation (23) to (25) become unsatisfiable is shown for the robot manipulator used in the experiments. In this example, the capsule is placed so that the capsule and actuator dipole moments are parallel and are also orthogonal to the relative position **p**. In this configuration, a change in magnetic force $\delta\mathbf{f_m}$ in the $\pm\hat{\mathbf{x}}$ direction requires rotating the actuator moment about the $\pm\hat{\mathbf{y}}$ axis. The necessary motion could be infeasible if the robot manipulator is in a singular configuration, such as a spherical wrist singularity where the $\hat{\mathbf{a}}_3$ and $\hat{\mathbf{a}}_5$ revolute axes of the manipulator's spherical wrist are parallel (as illustrated for the manipulator used herein).

which scales the applied magnetic force (6). Increasing the capsule's weight while keeping the actuator and capsule moment magnitudes constant decreases the equilibrium distance. If the apparent weight is increased, the

equilibrium distance can be kept constant by scaling the capsule or actuator dipole moment magnitudes (e.g. selecting a higher grade or increasing volume).

To simplify scaling analysis, we consider the 1D problem where the capsule is positioned immediately below the actuator magnet and is constrained to move with one DOF up or down, as illustrated in Figure 6. In the configuration shown, the attractive magnetic force directly opposes the capsule's apparent weight. In this configuration, the equilibrium separation distance is

$$\|\mathbf{p}\|_{\text{equal}} = \left(\frac{3\mu_0}{2\pi}\frac{\|\mathbf{m_a}\|\|\mathbf{m_c}\|}{\|\mathbf{f_w}\|}\right)^{1/4} \quad (35)$$

In this 1D analysis, the error in the estimated capsule position can be amplified by the derivative $\mathrm{d}\|\mathbf{f}\|/\mathrm{d}\|\mathbf{p}\|$ to approximate the resulting error in applied magnetic force. At the equilibrium distance, the derivative is given by

$$\frac{\mathrm{d}\|\mathbf{f}\|}{\mathrm{d}\|\mathbf{p}\|}\bigg|_{\|\mathbf{p}\| = \|\mathbf{p}\|_{\text{equal}}} = -4\left(\frac{2\pi}{3\mu_0}\frac{\|\mathbf{f_w}\|^5}{\|\mathbf{m_a}\|\|\mathbf{m_c}\|}\right)^{1/4} = -4\frac{\|\mathbf{f_w}\|}{\|\mathbf{p}\|_{\text{equal}}} \quad (36)$$

A plot of the equilibrium distance (35) and the force derivative (36) for varying $\|\mathbf{m_a}\|\|\mathbf{m_c}\|$ and $\|\mathbf{f_w}\|$ is shown in Figure 6(c) and (d), respectively. As shown, the equilibrium distance increases and the magnitude of the force derivative decreases when $\|\mathbf{f_w}\|$ decreases or $\|\mathbf{m_a}\|\|\mathbf{m_c}\|$ increases. For

(a) Side view (of applied forces)

(b) Front view (of dipole configuration)

(c) Equilibrium distance, $\|\mathbf{p}\|_{\text{equal}}$ (m)

(d) $\mathrm{d}\|\mathbf{f_m}\|/\mathrm{d}\|\mathbf{p}\|$ at equilibrium distance (mN/m)
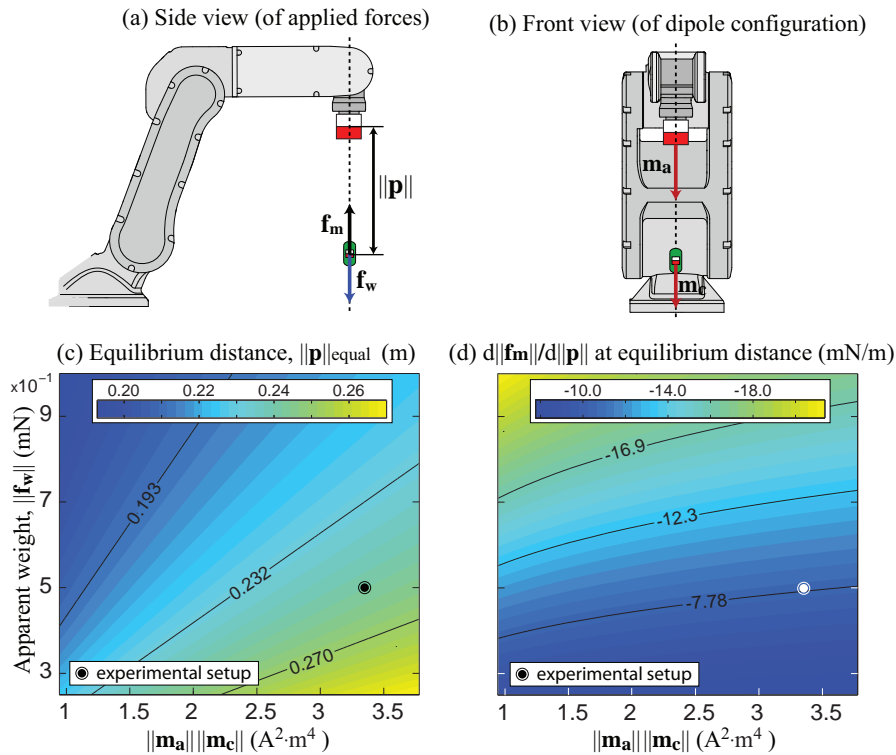
Fig. 6. The equilibrium distance $\|\mathbf{p}\|_{\text{equal}}$, where the apparent capsule weight is balanced by the attractive magnetic force, is shown in (a) for the configuration portrayed in (c) and (d), as a function of the product $\|\mathbf{m_a}\|\|\mathbf{m_c}\|$ and the apparent capsule weight $\|\mathbf{f_w}\|$. The derivative $\mathrm{d}\|\mathbf{f}\|/\mathrm{d}\|\mathbf{q}\|$ at the equilibrium distance, as a function of $\|\mathbf{m_a}\|\|\mathbf{m_c}\|$ and $\|\mathbf{f_w}\|$, is shown in (b). The equilibrium distance (0.251 m) and derivative (-8 mN/m) of the experimental setup used herein is shown to scale in (a) and (b).

the experimental setup used, the apparent capsule weight (0.5 mN) and $\|\mathbf{m_a}\|\|\mathbf{m_c}\|$ product (3.30 A^2·m^4) admit an equilibrium distance of 0.251 m (depicted in Figure 6(c)) and a force derivative of -8 mN/m (depicted in Figure 6(d)). In general, for any given capsule apparent weight $\|\mathbf{f_w}\|$, $\|\mathbf{m_a}\|\|\mathbf{m_c}\|$ can be increased by increasing the grade or volume of the actuator magnet to reduce the effects of capsule position uncertainty.

Scaling the product $\|\mathbf{m_a}\|\|\mathbf{m_c}\|$ does not affect the singular values of the nondimensional Jacobian $\tilde{J}_{\mathcal{FA}}$ (shown in Figures 3 and 4), since normalization by the applied magnetic force magnitude $\|\mathbf{f_m}\|$ removes the only dependence of $J_{\mathcal{FA}}$ on $\|\mathbf{m_a}\|\|\mathbf{m_c}\|$. This means that for a desired applied magnetic force, scaling $\|\mathbf{m_a}\|\|\mathbf{m_c}\|$ does not change the necessary magnitude of manipulator joint motion to obtain the same *percentage* change in the desired applied magnetic force. However, scaling $\|\mathbf{m_a}\|\|\mathbf{m_c}\|$ does change the *magnitude* of the applied magnetic force. It is easy to verify that the direction of the applied magnetic force (6) does not vary with $\|\mathbf{p}\|$. As a result, after scaling $\|\mathbf{m_a}\|\|\mathbf{m_c}\|$, the actuator magnet must move in a direction parallel to $\hat{\mathbf{p}}$ in order to keep the magnitude and direction of the applied magnetic force constant.

This is illustrated in Figure 7, which shows the labeled actuator magnet configurations necessary to apply the equivalently labeled total applied force for the same actuator magnet and capsule used in Figure 3. The actuator magnet configuration that achieves the same applied force when scaling $\|\mathbf{m_a}\|\|\mathbf{m_c}\|$ by a factor of two, four, and eight are shown and labeled with the corresponding scaling factor (except for pose '1' for which only the scaling factor two is shown, and pose '5' for which only the scaling factors two and four are shown). In Figure 7(a) and (b), the actuator magnet poses resulting from scaling are overlaid

on the maximum singular value of $\tilde{J}_{\mathcal{FA}}^{\dagger}$ from Figure 3(a) and (b), respectively. Scaling $\|\mathbf{p}\|$ to keep the applied force constant when scaling $\|\mathbf{m_a}\|\|\mathbf{m_c}\|$ causes the necessary actuator configurations that achieve the same desired forces to move into different regions of the robot manipulator's workspace. This could be problematic in the case of pose '12', for example, where scaling $\|\mathbf{m_a}\|\|\mathbf{m_c}\|$ by a factor of four causes the robot manipulator to enter a singularity.

Increasing the size of the actuator and capsule magnets increases the magnitude of their dipole moments and allows the capsule to be actuated where $\|\mathbf{p}\|$ is greater (see (35)), and the applied magnetic force is less sensitive to changes in $\|\mathbf{p}\|$ (see (36)). If the manipulator has velocity limits, then the actuator magnet volume should be selected so that the manipulator's velocity limits are not exceeded when compensating for typical disturbances in the capsule's position. However, when selecting the actuator and capsule magnets for a particular manipulation task, the selection of the product $\|\mathbf{m_a}\|\|\mathbf{m_c}\|$ should be guided using plots like Figure 7(a) and (b), to keep the robot manipulator from entering singularities or exceeding the manipulator's reachable workspace during the application of typical forces.

3. Experimental results and discussion

The mockup capsule is actuated in a tank of water by an axially magnetized, grade N42, cylindrical NdFeB magnet with a height of 31.75 mm, a diameter of 31.75 mm, and with a dipole moment of $\|\mathbf{m_a}\| = 26.2$ A·m^2, positioned by a Yaskawa-Motoman MH5 6-DOF robotic manipulator. The capsule contains a cube NdFeB permanent magnet with its dipole moment $\|\mathbf{m_c}\| = 0.126$ A·m^2 arranged parallel to the capsule's principal axis; the remainder of the capsule's volume is filled with air. The capsule's weight is
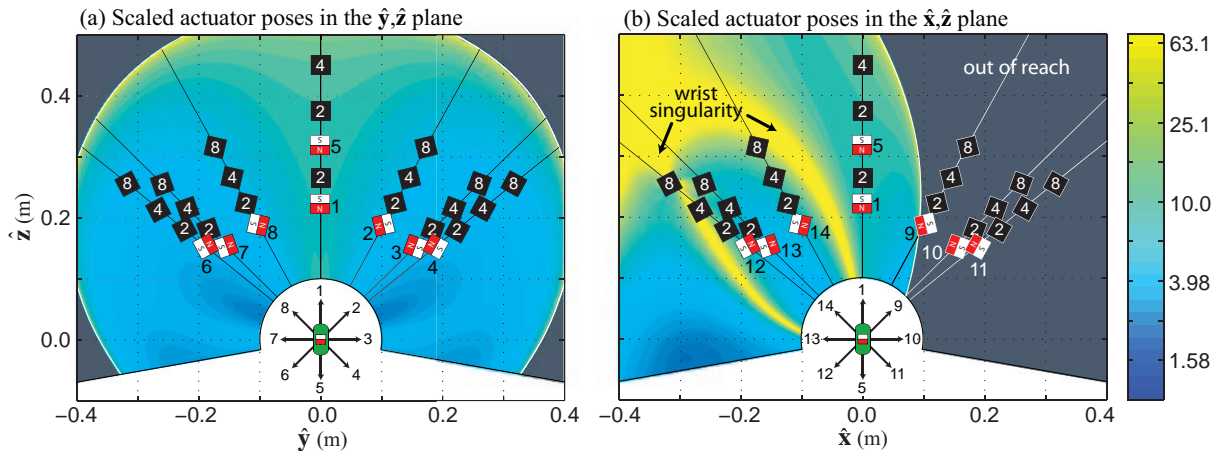

Fig. 7. Scaling the product $\|\mathbf{m_a}\|\|\mathbf{m_c}\|$ requires scaling the capsule–actuator separation distance $\|\mathbf{p}\|$ in order to keep the desired applied force constant (the position direction $\hat{\mathbf{p}}$ and actuator dipole moment heading $\hat{\mathbf{m}}_a$ remain unchanged). The labeled actuator magnet configurations that achieve the same (equivalently labeled) applied force when scaling $\|\mathbf{m_a}\|\|\mathbf{m_c}\|$ by a factor of two, four, and eight are shown with the corresponding scaling factor (except for pose '1' for which only the scaling factor two is shown, and pose '5' for which only the scaling factors two and four are shown). The actuator magnet configurations are overlaid on the maximum singular value of $\tilde{J}_{\mathcal{FA}}^{\dagger}$ in the $\hat{\mathbf{y}}, \hat{\mathbf{z}}$ and $\hat{\mathbf{x}}, \hat{\mathbf{z}}$ planes from Figure 3(a) and (b), respectively. The unscaled value of $\|\mathbf{m_a}\|\|\mathbf{m_c}\|$ is the same as that used in Figure 3 and the experimental results. Note that the color scale is logarithmic.
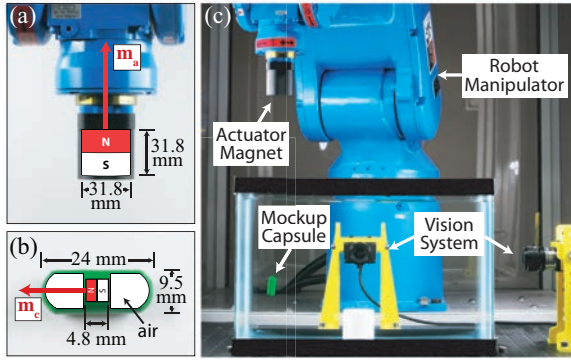
Fig. 8. The axially magnetized actuator magnet (a) is used to wirelessly control the mockup capsule endoscope (b) in a water-filled tank, using the 6-DOF robotic manipulator and vision system shown in (c).

0.0153 N and the buoyancy force in water is 0.0148 N. The position of the capsule is triangulated by two orthogonal Basler A602FC cameras, which are used with an extended Kalman filter for capsule-position feedback. Unless otherwise stated, the localization system's update frequency is 90 Hz. The experimental setup, consisting of the robot manipulator, vision system, mockup capsule, and the actuator magnet is shown in Figure 8.

A simple proportional-integral-derivative (PID) feedback controller (using the triangulated capsule position) with a gravity-compensating feed-forward term was implemented to servo the capsule to any desired position in the workspace. At every iteration, the PID controller takes as input a desired capsule position $\mathbf{p_{c,d}}$, an estimated capsule position $\bar{\mathbf{p}}_c$, and an estimated capsule spatial velocity $\dot{\bar{\mathbf{p}}}_c$, and produces a desired change in applied force $\delta\mathbf{f_d}$, which is then combined with a desired change in applied field heading $\delta\hat{\mathbf{h}}_d$ and converted into motion of the robotic manipulator by solving the constrained least-squares formulation (20) to (22). An estimate of the capsule's heading is obtained from the measured position using (1), and is controlled in an open-loop fashion. In this paper, we compute a desired change in field heading (which is equivalent to a desired change in capsule heading) as the difference between a desired capsule heading and an estimate of the

current capsule heading, which we assume to be small at each controller iteration. Due to a limitation of the commercial manipulator control system, the robot manipulator's position is updated at 25 Hz. A diagram of the controller is shown in Figure 9.

The theory presented herein, as well as our control system, is demonstrated by controlling the magnetic mockup capsule along multiple predefined trajectories. Figure 10(a) shows an image sequence of the capsule following a raster-scan trajectory where the capsule moves from right to left along a square-wave path with an amplitude of 25 mm and a period of 40 mm (see Extension 1). Such a trajectory could be used to perform automated visual coverage of a surface for inspection tasks. The desired square-wave trajectory and the actual paths traveled by the capsule while moving at desired spatial velocities of 2 mm/s, 4 mm/s, 8 mm/s and 16 mm/s are shown in Figure 10(b). In general, the trajectory tracking performance worsens with increasing desired spatial velocity. It is important to note that at high spatial velocities a fluidic torque can be generated that may cause the capsule's dipole moment $\mathbf{m_c}$ to become misaligned with the applied magnetic field $\mathbf{h}$. If this occurs, then the assumptions of Section 2 are violated and the actual applied magnetic force may deviate from that expected. This happens to the capsule when following the square-wave trajectory with a desired spatial velocity of 16 mm/s, causing the capsule to deviate wildly from that desired, which can be particularly observed in the $\hat{\mathbf{x}}$, $\hat{\mathbf{z}}$ plane.

Two additional maneuvers are demonstrated in Figure 11. In Figure 11(a), the capsule's heading is rotated from a down-pointing to a side-pointing configuration, while the feedback controller attempts to regulate the capsule's position to remain stationary (see Extension 2). Nonintuitively, the actuator magnet does not remain directly above the capsule during the transition. In Figure 11(b), the capsule's position follows a U-shaped trajectory while its heading remains constant (see Extension 3).

The vision system used to track the 3-DOF capsule position is not feasible for clinical use. Existing clinically relevant localization strategies include radio-frequency (RF) triangulation (Fischer et al., 2004), magnetic methods (Kim et al., 2010; Salerno et al., 2012; Di Natali et al.,
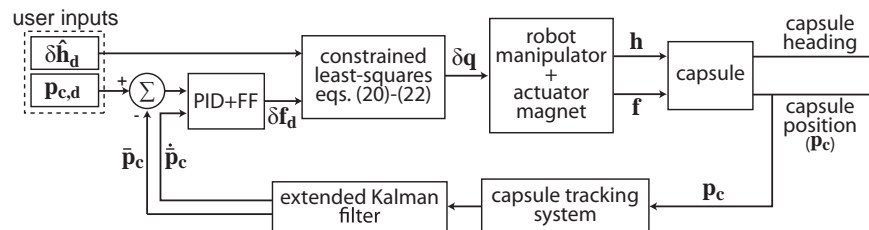

Fig. 9. A PID feedback controller, with a gravity-compensating feedforward (FF) term, governs the capsule position $\mathbf{p_c}$ while the capsule heading is controlled in an open-loop fashion. The PID controller takes as input a desired capsule position $\mathbf{p_{c,d}}$, an estimated capsule position $\bar{\mathbf{p}}_c$, and an estimated capsule spatial velocity $\dot{\bar{\mathbf{p}}}_c$, and produces a desired change in total applied force $\delta\mathbf{f_d}$. The desired change in applied force $\delta\mathbf{f_d}$ and the desired change in heading $\delta\hat{\mathbf{h}}_d$ is converted into a necessary change in robot manipulator joints $\delta\mathbf{q}$ by solving the formulation (20) to (22).
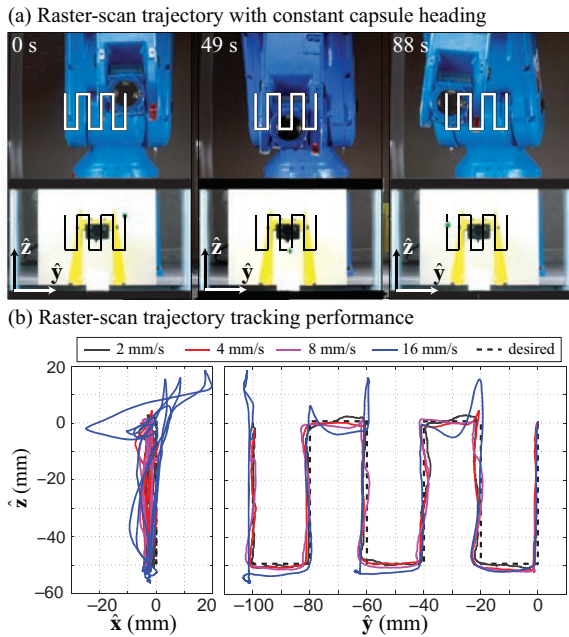
(a) Raster-scan trajectory with constant capsule heading

(b) Raster-scan trajectory tracking performance

Fig. 10. An image sequence of the capsule completing a raster-scan trajectory (moving from right to left) with a desired capsule spatial velocity of 4 mm/s is shown in (a), along with the approximate path taken by the actuator magnet. The capsule is oriented in the $\hat{\mathbf{x}}$ direction (toward the camera). The tracking performance of the control system for desired capsule spatial velocities ranging from 2 mm/s to 16 mm/s is shown in (b). With a desired spatial velocity of 16 mm/s, the raster-scan trajectory is completed in 35 s. Multimedia corresponding to (a) appears in Extension 1.

(a) Heading change while maintaining capsule position

(b) U-shaped trajectory while maintaining capsule heading

Fig. 11. The mockup capsule can be holonomically controlled with five DOFs. In (a), the capsule is controlled to adjust its heading while remaining stationary in space (see Extension 2). In (b), the capsule follows a U-shaped trajectory while maintaining a constant heading (see Extension 3). The approximate path taken by the actuator magnet is shown in both examples.

2013; Popek et al., 2013), and CT scan or X-ray fluoroscopy (Carpi and Pappone, 2009). In the previous experiments, the mockup capsule's position was localized at 90 Hz by the vision system. Clinically feasible localization methods may not provide the capsule's position at high rates (the method of Di Natali et al., 2013, can perform 3D position-tracking at approximately 50 Hz). The ability to actuate a mockup capsule with reduced 3D localization update frequencies is demonstrated in Figure 12, which shows the mockup capsule performing a remote-center-of-motion (RCM) maneuver, requiring the capsule's position to rotate around (while simultaneously pointing at) a fixed point in space. The update frequency of the tracking system (including the extended Kalman filter) was reduced to 60 Hz and 30 Hz, in order to simulate the update rate of a more clinically relevant localization method. Figure 12(a) shows images of the capsule performing the RCM maneuver with a 90 Hz localization rate, while Figure 12(b) shows the 3D position-tracking performance of the capsule for localization rates of 30, 60, and 90 Hz. The average position-tracking error for the localization rates of 30, 60, and 90 Hz is 2.8, 2.2, and 2.1 mm, respectively, with a standard deviation of 1.8, 1.2, and 1.0 mm, respectively. The capsule's heading-tracking performance is shown in Figure 12(c). The heading-tracking performance tends to
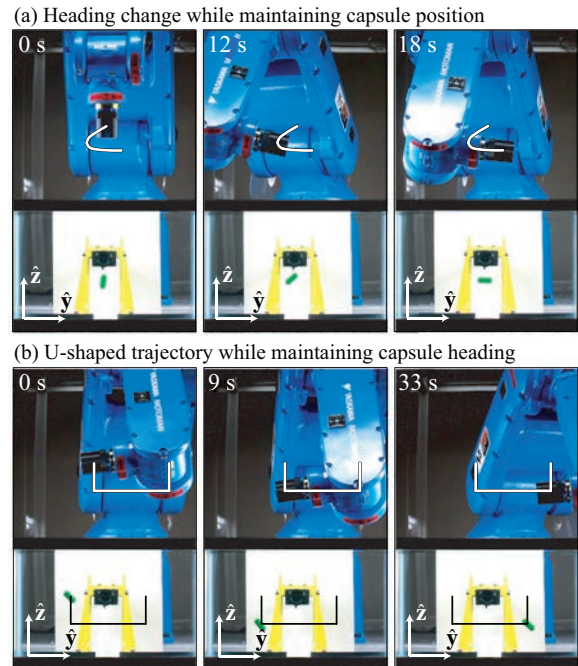
vary less with the localization frequency. The capsule moves at approximately 2 mm/s and completes the RCM maneuver in 62 s. A video of the RCM maneuver is shown in Extension 4.

We have found that deviation of the actuator magnet's field from that of a point-dipole has a profound effect on trajectory tracking performance, even for high localization frequencies. For the geometry of a stand-alone permanent magnet with the same geometry as the actuator used herein, it can be shown that the magnet's field differs from a point-dipole field by less than 1% provided $\|\mathbf{p}\| \geq 113$ mm (Petruska and Abbott, 2013). In typical operation $\|\mathbf{p}\|$ generally varies from 205 mm to 250 mm, making the field generated by the actuator magnet *alone* very close to that of a point-dipole. We have found, however, that the actual applied magnetic field includes a component caused by the presence of ferromagnetic material in the robot manipulator's wrist, which is magnetized due to close proximity with the actuator magnet. The magnetic field distortion becomes particularly evident in configurations where the capsule is desired to point in a direction orthogonal to gravity (e.g. the capsule configuration illustrated in Figure 4) and the robot manipulator's wrist moves closer to the mockup capsule.

This is demonstrated in Figure 13, which shows three poses of the capsule and robot manipulator for $\mathbf{m_c}$ parallel to the $-\hat{\mathbf{y}}$, $-\hat{\mathbf{z}}$, and $\hat{\mathbf{y}}$ directions in (a), (b), and (c),

(a) Remote-center-of-motion (RCM) maneuver

(b) RCM position-tracking with varying localization rates

(c) RCM heading-tracking with varying localization rates
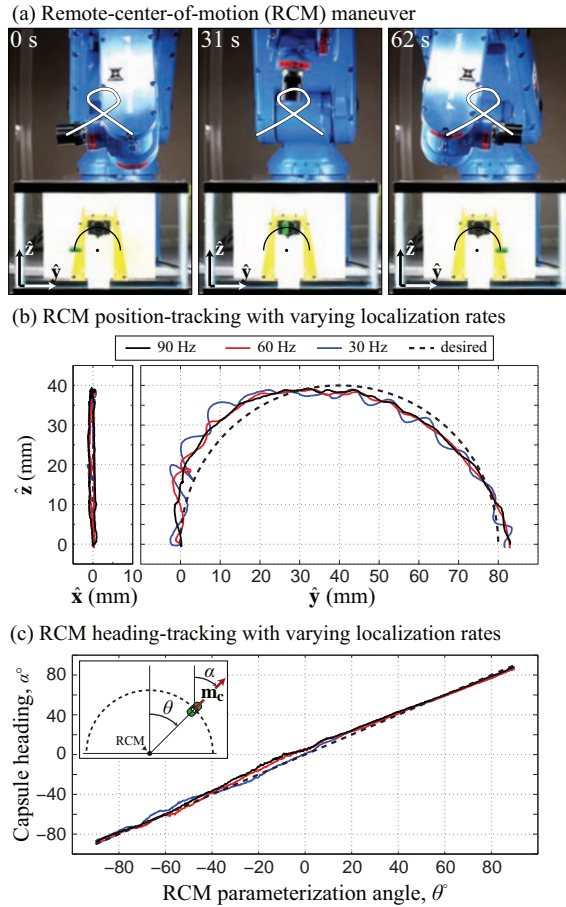

Fig. 12. The mockup capsule follows a desired remote-center-of-motion (RCM) maneuver in (a), with the approximate path taken by the actuator magnet shown. The position-following performance in the $\hat{\mathbf{x}},\hat{\mathbf{z}}$ and $\hat{\mathbf{y}},\hat{\mathbf{z}}$ planes, with the localization system tracking the capsule at 30, 60, and 90 Hz, is shown in (b). The heading-following performance of the mockup capsule (measured in the $\hat{\mathbf{y}},\hat{\mathbf{z}}$ plane) is shown in (c). The capsule heading is measured using the vision system but is controlled in an open-loop fashion. Multimedia corresponding to (a) appears in Extension 4.

respectively. In all three examples, the capsule is stationary in space, which indicates that the total force applied to the capsule is zero. In the example of Figure 13(a), a perfect dipole-field would require the actuator magnet to be positioned directly above the capsule (i.e. with no component of $\mathbf{p}$ in the $\hat{\mathbf{y}}$ direction). Although some error can be attributed to misalignment of the capsule's dipole moment $\mathbf{m_c}$ with the capsule's principal axis, the major source of error is due to the distortion in the magnetic field with the combined result causing the capsule to actually levitate approximately 21 mm from the position where the point-dipole model indicates it should. According to the point-dipole model, the total applied force is predicted to be $\mathbf{f} = [0, -7.6, 4.2]^\mathrm{T}$ mN in this configuration. Figure 13(c) demonstrates similar errors when the capsule is desired to point in the opposite
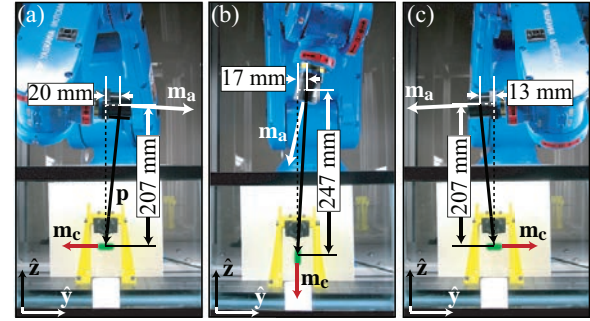

Fig. 13. Ferromagnetic material in the robot manipulator's wrist is magnetized by the actuator magnet, which causes the magnetic field applied to the capsule to be distorted from a point-dipole. In (a) and (c), the capsule is desired to levitate and point in the $-\hat{\mathbf{y}}$ and $+\hat{\mathbf{y}}$ directions, respectively. A perfect point-dipole field would require that the actuator magnet be placed directly above the capsule and pointed in the $+\hat{\mathbf{y}}$ and $-\hat{\mathbf{y}}$ directions, respectively. In (b), the capsule is desired to levitate while pointing in the $-\hat{\mathbf{z}}$ direction. A perfect point-dipole field would place the actuator magnet directly above the capsule and pointed in the $-\hat{\mathbf{z}}$ direction. In all three configurations, the point-dipole model predicts a non-zero applied force. The error in the magnetic field is accommodated by the PID controller.

direction of Figure 13(a) and the predicted force from the point-dipole model is $\mathbf{f} = [0, 0.1, 0.04]^\mathrm{T}$ mN.

Figure 13(b) shows an example where the capsule is desired to point in the $-\hat{\mathbf{z}}$ direction. In this configuration, the robot manipulator's wrist is positioned farthest from the capsule, and the capsule levitates approximately 7 mm from the point where the point-dipole model predicts. According to the point-dipole model, the total applied force is predicted to be $\mathbf{f} = [0, 1.9, 1.8]^\mathrm{T}$ mN. Despite the fact that the applied magnetic field deviates from that of a point-dipole in all three examples, the matrices $\partial\hat{\mathbf{h}}/\partial\mathbf{q}$ and $\partial\mathbf{f}/\partial\mathbf{q}$ are sufficiently accurate to enable the PID controller (see Figure 9) to reject disturbances caused by the modeling error. Although the disturbance demonstrated in Figure 13 is caused as a result of the field itself deviating from that expected, it can also be caused by an error in the mockup capsule's expected position (e.g. due to noise in the localization system). The fact that the capsule can still be controlled despite the distortion in the magnetic field indicates that the method presented herein can also be robust to error in the expected capsule's position obtained by a localization system. The closed-loop tracking error of a specific system is likely to be sensitive to the specific magnetic field distortions and the specific sources of localization error, and is left as an open question. If the capsule localization method relies on the magnetic field generated by the actuator magnet to be a perfect point-dipole field (e.g. Di Natali et al., 2013), then distortions in the magnetic field will effect localization, and the resulting effect on capsule actuation is also an open question. Removing the source of distortion and using a spherical permanent magnet (which generates a
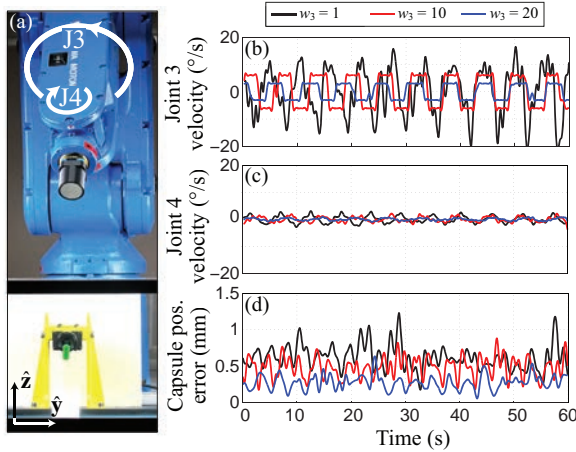
Fig. 14. The control strategy derived in Section 2.2 is demonstrated by levitating the capsule in a configuration that requires the robot manipulator to enter a wrist singularity (a). The angular velocities of joints 3 and 4 (labeled 'J3' and 'J4') are shown in (b) and (c), respectively, for three diagonal weight matrices: $W = \text{diag}([1, 1, 1, w_3, 1, 1]^T)$ with $w_3 = 1$, 10, and 20. With weight $w_3 = 1$, the velocity of joint 3 is not limited. With $w_3 = 10$ and 20, the absolute velocity of joint 3 is truncated to 7.06°/s and 3.58°/s, respectively. The capsule levitates as desired with the total position error (d) from the desired levitation position never exceeding 1.5 mm. Note that the most proximal joint is 'J0'.

near-exact point-dipole field) as the actuator magnet will mitigate these effects.

As described in Section 2.1, singularities in the robot manipulator's kinematics can impact capsule actuation. In Section 2.2, we derived a control strategy that relinquishes control over the capsule's heading while maintaining control over the applied magnetic force when the robot manipulator nears a singularity. Each iteration of the control method guarantees that the joint motion of the robot manipulator, $\delta\mathbf{q}$, will be limited by the constraint $\|W\delta\mathbf{q}\| \leq r$, where $W \in \mathbb{R}^{n \times n}$ is an invertible weight matrix. We test this control strategy by levitating the mockup capsule in a configuration where the capsule's dipole moment $\hat{\mathbf{m}}_c$ is rotated $10°$ around the $\hat{\mathbf{y}}$ axis (i.e. $\hat{\mathbf{m}}_c = [017, 0.98, 0]^T$). This configuration forces the robot manipulator into its spherical-wrist singularity (i.e. 'gimbal lock'), where axes $\hat{\mathbf{a}}_3$ and $\hat{\mathbf{a}}_5$ are parallel (see Figure 5).

Figure 14 shows the robot manipulator levitating the mockup capsule in the wrist-singularity configuration (Figure 14(a)) along with three plots that present the angular velocity of the third and fourth joints (labeled 'J3' and 'J4') in Figure 14(b) and (c), respectively, and the total position error of the capsule from the desired levitation position as a function of time in Figure 14(d). Three curves are plotted on each plot, which are obtained using a weight matrix $W = \text{diag}([1, 1, 1, w_3, 1, 1]^T)$ for $w_3 = 1$, 10, and 20, and with the constraint bound $r = 60°/s$. When $w_3 > 1$, the motion in the third joint is penalized more than others. As can be observed in Figure 14(b), the constraint $\|W\delta\mathbf{q}\| \leq r$
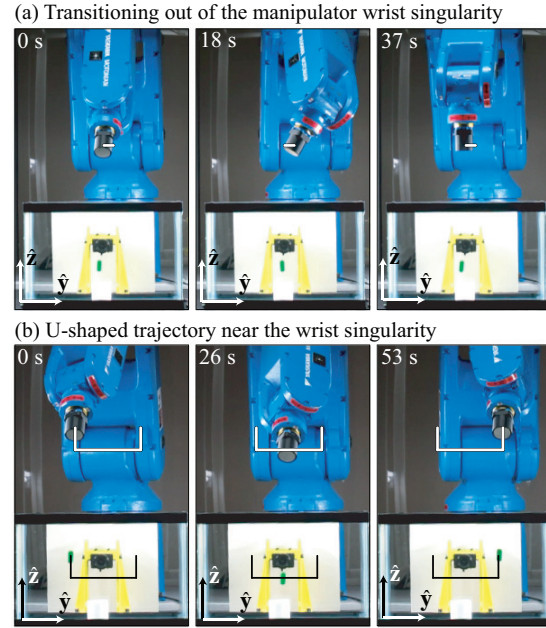

Fig. 15. In (a), the user commands the capsule to rotate from a configuration that forces the robot manipulator into its wrist singularity, to a configuration with the capsule pointed in the $-\hat{\mathbf{z}}$ direction, while maintaining the capsule's position in space. Rather than immediately rotating the third joint to accommodate the desired capsule motion, the control method guides the manipulator to first rotate the capsule about the $\hat{\mathbf{z}}$ axis to reduce net manipulator motion, while maintaining control over the capsule's position. In (b), the mockup capsule follows a U-shaped trajectory with the manipulator near its wrist singularity, which demonstrates 3-DOF control over the mockup capsule's position. The approximate path taken by the actuator magnet is shown in both examples. Multimedia corresponding to (a) and (b) appear in Extensions 5 and 6, respectively.

does not limit the third joint's motion when $w_3 = 1$. When $w_3 = 10$ and 20, the third joint's absolute velocity is truncated to 7.06°/s and 3.58°/s, respectively. As can be observed in Figure 14(c), the fourth joint moves very little and keeps the manipulator in the wrist singularity position. Figure 14(d) shows that the error between the desired levitation position and the actual capsule position never exceeds 1.5 mm, indicating that the capsule levitates as desired despite the robot manipulator's singularity, and that control over the magnetic force is maintained. Interestingly, the position error reduces as the weight w_3 increases, which indicates that rapid motion of joint 3 was contributing to the capsule's motion in an undesired way during levitation with smaller values of w_3.

Figure 15(a) shows the capsule transitioning from the configuration that forces the robot manipulator to enter its wrist singularity, to a configuration where the capsule points in the $-\hat{\mathbf{z}}$ direction by rotating the desired capsule direction $10°$ around the $-\hat{\mathbf{y}}$ axis, while simultaneously keeping the capsule's position in space stationary (with $w_3 = 20$). In the initial robot manipulator configuration at time $t = 0$ s, the desired change in the capsule direction

would require the third joint of the robot manipulator to rapidly rotate 90° to align the manipulator's $\hat{\mathbf{a}}_4$ axis in the $\hat{\mathbf{y}}$ direction. Rather than rapidly rotating the third joint, the constraint $\|W\delta\mathbf{q}\| \leq r$ penalizes the third joint's velocity and forces the manipulator to first rotate the capsule about the $\hat{\mathbf{z}}$ axis (which can be seen at $t = 18$ s) before rotating about the $\hat{\mathbf{y}}$ axis as desired. This demonstrates the ability of the controller to seamlessly balance desired changes in the capsule's configuration that may conflict with the robot manipulator's kinematics in a singularity. A video of the maneuver is shown in Extension 5.

Figure 15(b) shows the mockup capsule following a U-shaped trajectory (similar to that in Figure 11(b)), with the desired capsule dipole moment pointing in the direction that forces the manipulator nearly into its wrist singularity throughout the full trajectory (see Extension 6). This demonstrates the ability to control applied magnetic force despite robot manipulator singularities.

The stability of the mockup capsule under the control of the methods presented is difficult to study due to the nonlinearity of the applied magnetic field, nonlinearities resulting from the constraints of the formulation (20) to (22), and, in our case, velocity limitations of the manipulator. However, provided the magnetic torque dominates the mockup capsule's rotational dynamics and the actuator magnet is quasistatic, the applied magnetic torque will always stably align the capsule's dipole moment with the applied dipole field. In general, robotic manipulators tend to be bandwidth-limited. In the experiments, water provided damping that ensures stability in the capsule's position. Actuating the capsule in air with little damping would be difficult using a commercial manipulator. Future work should include further study of stability and robustness.

The experiments presented herein demonstrated the control of a 24-mm-long capsule-shaped untethered magnetic device intended to demonstrate use for capsule endoscopy of the stomach. Other areas where the control of an untethered magnetic device could be useful include human vasculature (Nelson et al., 2010). The effects of scaling down the size of an untethered magnetic device (to fit inside human vasculature) on magnetic manipulation can be studied using (35) and (36) in the 1D example presented in Section 2.3. If the dimensions of the untethered device are scaled down by a factor of s, then the device's volume scales as a factor of s^3, which subsequently makes the device's apparent weight $\|\mathbf{f_w}\|$ and the magnitude of the device's dipole moment $\|\mathbf{m_c}\|$ also scale as s^3. The result is that the equilibrium distance $\|\mathbf{p}\|_{\text{equal}}$, given by (35), remains unchanged. The force derivative (36) will decrease as s^3, however, the same *percentage* change in desired force will require the same magnitude of robot motion.

If the application requires the percentage change in desired applied force to vary as the problem is scaled down, then the strength of the actuator magnet $\|\mathbf{m_a}\|$ can be adjusted (e.g. by increasing the actuator magnet's volume) to keep the necessary magnitude of robot motion constant. This indicates that the scaling of the actuator magnet's magnetic field will not preclude the use of our methods for operating scaled-down untethered devices. The most likely limiting factors in operation in vasculature will be the pulsatile nature of the blood-flow velocity, which will require the use of a high-bandwidth robot system and will likely violate the quasistatic assumption made in Section 2. Localizing the untethered magnetic device in vasculature at the rates needed for stable magnetic control will be challenging as well (Nelson et al., 2010).

4. Conclusion

We have demonstrated 3-DOF position and 2-DOF orientation control of a mockup magnetic capsule endoscope using a single permanent magnet positioned by a 6-DOF serial-link manipulator, while only requiring the 3-DOF capsule position to be measured. We have studied the kinematics of manipulating an untethered magnetic device using a single permanent magnet as the end-effector of a robot manipulator, and introduced a control method that seamlessly sacrifices control over the capsule's heading in order to maintain control over the capsule's position when the robot manipulator enters a kinematic singularity. We have demonstrated our method's robustness to a control rate of 25 Hz, a localization rate of 30 Hz, deviation in the applied magnetic field from that expected, and the presence of manipulator singularities. Although our method has application in magnetic capsule endoscopy of a fluid-distended stomach, the methods can be applied to magnetic manipulation in general.

References

Arezzo A, Menciassi A, Valdastri P, et al. (2013) Experimental assessment of a novel robotically-driven endoscopic capsule compared to traditional colonoscopy. *Digestive and Liver Disease* 45(8): 657–662.

Berkelman P and Dzadovsky M (2013) Magnetic levitation over large translation and rotation ranges in all directions. *IEEE/ASME Transactions on Mechatronics* 18(1): 44–52.

Carpi F and Pappone C (2009) Magnetic maneuvering of endoscopic capsules by means of a robotic navigation system. *IEEE Transactions on Biomedical Engineering* 56(5): 1482–1490.

Chiaverini S, Siciliano B and Egeland O (1994) Review of the damped least-squares inverse kinematics with experiments on an industrial robot manipulator. *IEEE Transactions on Control Systems Technology* 2(2): 123–134.

Ciuti G, Donlin R, Valdastri P, et al. (2010a) Robotic versus manual control in magnetic steering of an endoscopic capsule. *Endoscopy* 42(2): 148–152.

Ciuti G, Valdastri P, Menciassi A, et al. (2010b) Robotic magnetic steering and locomotion of capsule endoscope for diagnostic and surgical endoluminal procedures. *Robotica* 28(2): 199–207.

Diller E, Giltinan J and Sitti M (2013) Independent control of multiple magnetic microrobots in three dimensions. *The International Journal of Robotics Research* 32(5): 614–631.

Di Natali C, Beccani M and Valdastri P (2013) Real-time pose detection for magnetic medical devices. *IEEE Transactions on Magnetics* 49(7): 3524–3527.

Doty KL, Melchiorri C and Bonivento C (1993) A theory of generalized inverses applied to robotics. *The International Journal of Robotics Research* 12(1): 1–19.

Fischer D, Schreiber R, Levi D, et al. (2004) Capsule endoscopy: The localization system. *Gastrointestinal Endoscopy Clinics of North America* 14(1): 25–31.

Fountain TWR, Kailat PV and Abbott JJ (2010) Wireless control of magnetic helical microrobots using a rotating-permanent-magnet manipulator. In: *Proceedings of the IEEE international conference on robotics and automation*, pp. 576–581.

Furlani EP (2001) *Permanent Magnet and Electromechanical Devices: Materials, Analysis, and Applications*. 1st edn. San Diego, CA: Academic Press.

Gang ES, Nguyen BL, Shachar Y, et al. (2011) Dynamically shaped magnetic fields: Initial animal validation of a new remote electrophysiology catheter guidance and control system. *Circulation: Arrhythmia and Electrophysiology* 4(5): 770–777.

Gauthier M and Piat E (2006) Control of a particular micro-macro positioning system applied to cell micromanipulation. *IEEE Transactions on Automation Science and Engineering* 3(3): 264–271.

Gillies GT, Ritter RC, Broaddus WC, et al. (1994) Magnetic manipulation instrumentation for medical physics research. *Review of Scientific Instruments* 65(3): 533–562.

Hager WW (2001) Minimizing a quadratic over a sphere. *SIAM Journal on Optimization* 12(1): 188–208.

Hou MT, Shen HM, Jiang GL, et al. (2010) A rolling locomotion method for untethered magnetic microrobots. *Applied Physics Letters* 96: 024102–024105.

Ishiyama K, Arai KI, Sendoh M, et al. (2003) Spiral-type micromachine for medical applications. *Journal of Micromechatronics* 2(1): 77–86.

Jiang GL, Guu YH, Lu CN, et al. (2010) Development of rolling magnetic microrobots. *Journal of Micromechanics and Microengineering* 20: 085042.

Keller H, Juloski A, Kawano H, et al. (2012) Method for navigation and control of a magnetically guided capsule endoscope in the human stomach. In: *Proceedings of the IEEE international conference on biomedical robotics and biomechatronics*, pp. 859–865.

Keller J, Fibbe C, Volke F, et al. (2010) Remote magnetic control of a wireless capsule endoscope in the esophagus is safe and feasible: Results of a randomized, clinical trial in healthy volunteers. *Gastrointestinal Endoscopy* 72(5): 941–946.

Keller J, Fibbe C, Volke F, et al. (2011) Inspection of the human stomach using remote-controlled capsule endoscopy: A feasibility study in healthy volunteers (with videos). *Gastrointestinal Endoscopy* 73(1): 22–28.

Kim J, Kwon Y and Hong Y (2012) Automated alignment of rotating magnetic field for inducing a continuous spiral motion on a capsule endoscope with a twistable thread mechanism. *International Journal of Precision Engineering and Manufacturing* 13(3): 371–377.

Kim MG, Hong YS and Lim EJ (2010) Position and orientation detection of capsule endoscopes in spiral motion. *International Journal of Precision Engineering and Manufacturing* 11(1): 31–37.

Kummer MP, Abbott JJ, Kratochvil BE, et al. (2010) OctoMag: An electromagnetic systems for 5-DOF wireless micromanipulation. *IEEE Transactions on Robotics* 26(6): 1006–1017.

Lien G, Liu C, Jiang J, et al. (2012) Magnetic control system targeted for capsule endoscopic operations in the stomach: Design, fabrication, and in vitro and ex vivo evaluations. *IEEE Transactions on Biomedical Engineering* 59(7): 2068–2079.

Mahoney AW and Abbott JJ (2011) Managing magnetic force applied to a magnetic device by a rotating dipole field. *Applied Physics Letters* 99: 134103–134106.

Mahoney AW and Abbott JJ (2013) 5-DOF manipulation of a magnetic capsule in fluid using a single permanent magnet: Proof-of-concept for stomach endoscopy. In: *Proceedings of the 6th Hamlyn symposium on medical robotics*, pp. 114–115.

Mahoney AW and Abbott JJ (2014a) 5-DOF manipulation of an untethered magnetic device in fluid using a single permanent magnet. In: *Proceedings of robotics: Science and systems*.

Mahoney AW and Abbott JJ (2014b) Generating rotating magnetic fields with a single permanent magnet for propulsion of untethered magnetic devices in a lumen. *IEEE Transactions on Robotics* 30(2): 411–420.

Mahoney AW, Nelson ND, Parsons EM, et al. (2012) Non-ideal behaviors of magnetically driven screws in soft tissue. In: *Proceedings of the IEEE/RSJ international conference on intelligent robots and systems*, pp. 3559–3564.

Mahoney AW, Sarrazin JC, Bamberg E, et al. (2011) Velocity control with gravity compensation for magnetic helical microswimmers. *Advanced Robotics* 25(8): 1007–1028.

Mahoney AW, Wright SE and Abbott JJ (2013) Managing the attractive magnetic force between an untethered magnetically actuated tool and a rotating permanent magnet. In: *Proceedings of the IEEE international conference on robotics and automation*, pp. 5346–5351.

Martel S, Mathieu JB, Felfoul O, et al. (2007) Automatic navigation of an untethered device in the artery of a living animal using a conventional clinical magnetic resonance imaging system. *Applied Physics Letters* 90: 114105–114108.

Mewes PW, Foertsch S, Juloski AL, et al (2013) Chromoendoscopy in magnetically guided capsule endoscopy. *BioMedical Engineering OnLine* 12(52): 1–16.

Nelson BJ, Kaliakatsos IK and Abbott JJ (2010) Microrobots for minimally invasive medicine. *Annual Review of Biomedical Engineering* 12: 55–85.

Nguyen BL, Merino JL and Gang ES (2010) Remote navigation for ablation procedures – A new step forward in the treatment of cardiac arrhythmias. *European Cardiology* 6: 50–56.

Petruska AJ and Abbott JJ (2013) Optimal permanent-magnet geometries for dipole field approximation. *IEEE Transactions on Magnetics* 49(2): 811–819.

Popek KM, Mahoney AW and Abbott JJ (2013) Localization method for a magnetic capsule endoscope propelled by a rotating magnetic dipole field. In: *Proceedings of the IEEE international conference on robotics and automation*, pp. 5328–5333.

Rey JF, Ogata H, Hosoe N, et al. (2010) Feasibility of stomach exploration with a guided capsule endoscope. *Endoscopy* 42(7): 541–545.

Rey JF, Ogata H, Hosoe N, et al. (2012) Blinded non-randomized comparative study of gastric examination with a magnetically

guided capsule endoscope (MGCE) and standard videoendoscope. *Gastrointestinal Endoscopy* 75(2): 373–381.

Salerno M, Ciuti G, Lucarini G, et al. (2012) A discrete-time localization method for capsule endoscopy based on on-board magnetic sensing. *Measurement Science and Technology* 23(01570): 1–10.

Schuerle S, Erni S, Flink M, et al. (2013) Three-dimensional magnetic manipulation of micro- and nanostructures for applications in life sciences. *IEEE Transactions on Magnetics* 49(1): 321–330.

Sciavicco L and Siciliano B (2000) *Modeling and Control of Robot Manipulators*. 2nd edn. London: Springer-Verlag.

Swain P, Toor A, Volke F, et al. (2010) Remote magnetic manipulation of a wireless capsule endoscope in the esophagus and stomach of humans (with videos). *Gastrointestinal Endoscopy* 71(7): 1290–1293.

Tognarelli S, Castelli V, Ciuti G, et al. (2012) Magnetic propulsion and ultrasound tracking of endovascular devices. *Journal of Robotic Surgery* 6(1): 5–12.

Ullrich F, Bergeles C, Pokki J, et al. (2013) Mobility experiments with microrobots for minimally invasive intraocular surgery. *Investigative Ophthalmology & Visual Science* 54(4): 2853–2863.

Valdastri P, Ciuti G, Verbeni A, et al. (2012a) Magnetic air capsule robotic system: Proof of concept of a novel approach for painless colonoscopy. *Surgical Endoscopy* 26(5): 1238–1246.

Valdastri P, Simi M and Webster RJ III (2012b) Advanced technologies for gastrointestinal endoscopy. *Annual Review of Biomedical Engineering* 14: 397–429.

Wampler CW (1986) Manipulator inverse kinematic solutions based on vector formulations and damped least-squares methods. *IEEE Transactions on Systems, Man and Cybernetics* 16(1): 93–101.

Yim S and Sitti M (2012) Design and rolling locomotion of a magnetically actuated soft capsule endoscope. *IEEE Transactions on Robotics* 28(1): 183–194.

Zhang L, Abbott JJ, Dong LX, et al. (2009) Artificial bacterial flagella: Fabrication and magnetic control. *Applied Physics Letters* 94: 064107–064110.

Appendix A: Index to Multimedia Extensions

Archives of IJRR multimedia extensions published prior to 2014 can be found at http://www.ijrr.org, after 2014 all videos are available on the IJRR YouTube channel at http://www.youtube.com/user/ijrrmultimedia

Table of Multimedia Extensions

Extension	Media type	Description
1	Video	Demonstrating position control with a raster-scan trajectory.
2	Video	Demonstrating heading control while keeping position constant.
3	Video	Demonstrating position control with a U-shaped trajectory.
4	Video	Demonstrating position and heading control with an RCM maneuver.
5	Video	Demonstrating a transition out of a manipulator singularity.
6	Video	Demonstrating position control near a manipulator singularity.

Appendix B: Skew-symmetric matrix implementation of the cross-product operation

$S(\mathbf{v})$ maps $\mathbf{v} \in \mathbb{R}^3$ to $S(\mathbf{v}) \in so(3)$:

$$S(\mathbf{v}) = \begin{bmatrix} 0 & -\mathbf{v}_z & \mathbf{v}_y \\ \mathbf{v}_z & 0 & -\mathbf{v}_x \\ -\mathbf{v}_y & \mathbf{v}_x & 0 \end{bmatrix} \tag{37}$$

where $\mathbf{v}_x$, $\mathbf{v}_y$, $\mathbf{v}_z$ are the scalar components of the vector $\mathbf{v}$ in the coordinate directions $\hat{\mathbf{x}}$, $\hat{\mathbf{y}}$, and $\hat{\mathbf{z}}$, respectively.

Appendix C: Explicit representation of $J_{\mathcal{F}}(\mathbf{p}, \hat{\mathbf{m}}_\mathbf{a})$

The Jacobian matrix $J_{\mathcal{F}}(\mathbf{p}, \hat{\mathbf{m}}_\mathbf{a})$ is given by

$$J_{\mathcal{F}}(\mathbf{p}, \hat{\mathbf{m}}_\mathbf{a}) = \begin{bmatrix} F_p & F_m \\ H_p & H_m \end{bmatrix} \tag{38}$$

where the submatrices F_p, F_m, H_p, and H_m are members of $\mathbb{R}^{3 \times 3}$, and are defined as

$$H_m = \frac{\partial \hat{\mathbf{h}}}{\partial \hat{\mathbf{m}}_\mathbf{a}} \tag{39}$$

$$H_p = \frac{\partial \hat{\mathbf{h}}}{\partial \mathbf{p}} \tag{40}$$

$$F_m = \frac{\partial \mathbf{f}}{\partial \hat{\mathbf{m}}} + \frac{\partial \mathbf{f}}{\partial \hat{\mathbf{h}}} \frac{\partial \hat{\mathbf{h}}}{\partial \hat{\mathbf{m}}} \tag{41}$$

$$F_p = \frac{\partial \mathbf{f}}{\partial \mathbf{p}} + \frac{\partial \mathbf{f}}{\partial \hat{\mathbf{h}}} \frac{\partial \hat{\mathbf{h}}}{\partial \mathbf{p}} \tag{42}$$

$$\frac{\partial \mathbf{f}}{\partial \mathbf{p}} = \frac{\gamma}{\|\mathbf{p}\|^5} \left(Y - 5\hat{\mathbf{p}}\hat{\mathbf{p}}^\mathrm{T} Y - 5Y\hat{\mathbf{p}}\hat{\mathbf{p}}^\mathrm{T} - 5\|D\hat{\mathbf{m}}_\mathbf{a}\|\hat{\mathbf{p}}\hat{\mathbf{p}}^\mathrm{T} \right) \tag{43}$$

$$\frac{\partial \mathbf{f}}{\partial \hat{\mathbf{h}}} = -\frac{\gamma}{\|\mathbf{p}\|^4} \left(\hat{\mathbf{m}}_\mathbf{a}\hat{\mathbf{p}}^\mathrm{T} + \hat{\mathbf{p}}\hat{\mathbf{m}}_\mathbf{a}^\mathrm{T} + (\hat{\mathbf{m}}_\mathbf{a}^\mathrm{T}\hat{\mathbf{p}})Z \right) S(\hat{\mathbf{h}})^2 \tag{44}$$

$$\frac{\partial \mathbf{f}}{\partial \hat{\mathbf{m}}_\mathbf{a}} = -\frac{\gamma}{\|\mathbf{p}\|^4} \left(\hat{\mathbf{h}}\hat{\mathbf{p}}^\mathrm{T} + \hat{\mathbf{p}}\hat{\mathbf{h}}^\mathrm{T} + (\hat{\mathbf{h}}^\mathrm{T}\hat{\mathbf{p}})Z \right) S(\hat{\mathbf{m}}_\mathbf{a})^2 \tag{45}$$

$$\frac{\partial \hat{\mathbf{h}}}{\partial \mathbf{p}} = \frac{3}{\|D\hat{\mathbf{m}}_\mathbf{a}\|\|\mathbf{p}\|} S(\hat{\mathbf{h}})^2 \left((\hat{\mathbf{p}}^\mathrm{T}\hat{\mathbf{m}}_\mathbf{a})I + \hat{\mathbf{p}}\hat{\mathbf{m}}_\mathbf{a}^\mathrm{T} \right) S(\hat{\mathbf{p}})^2 \tag{46}$$

$$\frac{\partial \hat{\mathbf{h}}}{\partial \hat{\mathbf{m}}_\mathbf{a}} = -\frac{1}{\|D\hat{\mathbf{m}}_\mathbf{a}\|} S(\hat{\mathbf{h}})^2 D \tag{47}$$

$$\gamma = \frac{3\mu_0 \|\mathbf{m}_\mathbf{a}\|\|\mathbf{m}_\mathbf{c}\|}{4\pi} \tag{48}$$

$$Y = \hat{\mathbf{m}}_\mathbf{a}\hat{\mathbf{h}}^\mathrm{T} + \hat{\mathbf{h}}\hat{\mathbf{m}}_\mathbf{a}^\mathrm{T} + (\hat{\mathbf{h}}^\mathrm{T} Z\hat{\mathbf{m}}_\mathbf{a})I \tag{49}$$

$$D = 3\hat{\mathbf{p}}\hat{\mathbf{p}}^\mathrm{T} - I \tag{50}$$

$$Z = I - 5\hat{\mathbf{p}}\hat{\mathbf{p}}^\mathrm{T} \tag{51}$$